Deformation-induced melting in the margins of the West-Antarctic ice streams

Jenny Suckale[1], John D. Platt[2], Thibaut Perol[2] and James R. Rice[2,3]

———

[1]Department of Geophysics, Stanford

University, Palo Alto, California USA.

[2]School of Engineering and Applied

Sciences, Harvard University, Cambridge,

Massachusetts, USA.

[3]Department of Earth and Planetary

Sciences, Harvard University, Cambridge,

Massachusetts, USA.

Abstract.   Flow of glacial ice in the West Antarctic Sheet localizes in narrow bands of fast flowing ice streams bordered by ridges of nearly stagnant ice, but our understanding of the physical processes that generate this morphology is incomplete. Here, we study the thermal and mechanical properties of ice-stream margins, where flow transitions from rapid to stagnant over a few kilometers. Our goal is to explore under which conditions the intense shear deformation in the margin may lead to deformation-induced melting. We propose a 2D model that represents a cross-section through the ice-stream margin perpendicular to the downstream flow direction. We limit temperature to the melting point to estimate melt rates based on latent heat. Using rheology parameters as constrained by laboratory data and observations, we conclude that a zone of temperate ice is likely to form in active shear margins.

1. Introduction

The West-Antarctic Ice Sheet is thought to lose over 80% of its mass [*Bamber et al.*, 2000] through outlet glaciers and arterial drainage routes called ice streams, which are typically about a kilometer thick, tens of kilometers wide and hundreds of kilometers long. Contrary to outlet glaciers, topography cannot fully explain the location of the fast-flowing ice streams in the Ross Ice Shelf, Antarctica [*Shabtaie and Bentley*, 1987, 1988]. Further evidence that ice-stream width is not controlled by topography alone comes from evidence that some margins have shifted in the past [*Jacobel et al.*, 1996; *Clarke et al.*, 2000; *Fahnestock et al.*, 2000; *Jacobel et al.*, 2000] or are migrating currently [*Bindschadler and Vornberger*, 1998; *Harrison et al.*, 1998; *Echelmeyer and Harrison*, 1999]. These observations suggest that a physical mechanism must exist that selects the location of the margin and the flow speed of the stream self-consistently.

The Ross Ice Streams rest on weak and unconsolidated sediment, commonly referred to as till, which overlays former seafloor [*Dreimanis*, 1988; *Tulaczyk et al.*, 1998]. Drilling into several active ice streams has confirmed near-lithostatic fluid pressure in the till below the ice streams [*Kamb*, 1991, 2001], and inverse methods have shown that the till layer is nearly everywhere weak [*Joughin et al.*, 2004]. These findings imply that only a very modest shear stress can be supported by the bed and highlight that till deformation is probably the primary mechanism that allows ice streams to move rapidly despite relatively small gravitational stresses [*Alley et al.*, 1986]. Measurements of shear stresses in the margins of the Ross Ice Streams [*Joughin et al.*, 2002] and a laboratory study of ice cores retrieved from depth [*Jackson and Kamb*, 1997] confirmed that a significant portion of

the driving stress is balanced by stresses on an approximately vertical interface parallel

to the edge of the ice stream. We refer to these lateral boundaries of ice streams, where

the surface velocity drops by two to three orders of magnitude over as little as a few

kilometers, as the shear margins.

While force-balance considerations clarify that shear margins play an important role

in ice-stream dynamics [*Whillans and Van Der Veen*, 1993; *Jackson and Kamb*, 1997;

Harrison et al., 1998; *Whillans and Van der Veen*, 2001; *Joughin et al.*, 2004], if probably

to a different degree for different streams [*Raymond*, 2000], they do not offer any direct

insights into the mechanism through which the margin affects the ice-stream flow. One

possibility is that shear margins represent not only the transition from fast to slow flow,

but may also coincide with the boundary between temperate and frozen conditions at the

bed [*Jacobson and Raymond*, 1998; *Schoof*, 2012]. One problem with this idea is that

even a small perturbation in ice-stream width would lead to either run-away growth or to

stoppage of an ice stream [*Jacobson and Raymond*, 1998]. *Schoof* [2004] questioned the

assumption that the transition between a temperate and a frozen bed determines, or even

coincides with, the position of the shear margin. As previously suggested by *Raymond*

[1996], *Schoof* [2004] invokes a spatially variable yield stress in the till layer, analogous to

Barenblatt-Dugdale concepts in fracture mechanics (e.g., *Rice* [1968a, b]), but does not

offer an explanation for the assumed functional forms of the yield stress along the glacial

bed.

The goal of this study is to investigate the possibility of deformation-induced melting

in active shear margins. There are two reasons why melting and the associated presence

of meltwater in ice-stream margins might have important consequences for the dynamics

60 of ice streams. First, glacial till can be approximated as a Coulomb plastic material

61 with a yield strength that is strongly dependent on porosity, which is controlled by the

62 water content for full saturation [*Iverson et al.*, 1998; *Tulaczyk*, 1999; *Rathbun et al.*,

63 2008] and diminishes with effective pressure [*Kamb*, 1991; *Iverson et al.*, 1998; *Tulaczyk*

64 *et al.*, 2000] in agreement with critical-state soil mechanics (e.g., *Schofield and Wroth*

65 [1968]). The sensitive dependence of shear strength on water content suggests that the

66 spatial variability of basal stress and the positions of the shear margins could be intricately

67 linked to meltwater generation. Second, if significant quantities of meltwater are produced

68 in the margin, the water may accumulate in a channelized drainage system as pointed out

69 by *Perol and Rice* [2011]. The presence of a channel alters both the basal stresses outside

70 of it and the pore-pressure distribution in its vicinity, which could contribute to locking

71 of the bed of a widening stream.

72 The possibility that the shear margins of active ice streams may be temperate has been

73 pointed out before [*Jacobson and Raymond*, 1998; *Beem et al.*, 2010], but it remains un-

74 clear how pervasive melting is. *Perol and Rice* [2014] suggested that the shear-strain rates

75 measured by *Joughin et al.* [2002] for the five Ross Ice Streams are consistent with internal

76 melting for all stream margins except the currently inactive Kamb Ice Stream. However,

77 their model based on a 1D heat-transfer model was not versatile enough to include ice

78 advection perpendicular to the margin. While observational evidence constraining the

79 thermal properties of shear margins at depth is scarce, *Clarke et al.* [2000] identified a

80 prominent bottom diffractor extending to about 230 m above the bed in the ice sheet

81 close to Unicorn ridge (Figure 1), which they interpreted as a delineation of a zone of wet

82 and reflective ice. Further, drilling into the currently inactive Kamb Ice Stream margin

revealed flowing water in a 1.6 m cavity between the bottom of the ice sheet and its bed

[*Vogel et al.*, 2005].

Here, we devise a 2D thermomechanical model of an ice stream moving over a plastic bed

in steady state. We consider a cross-section through the ice-stream margin perpendicular

to the downstream flow direction and analyze the effect of the anti-plane shear stress

components on the mechanical equilibrium and energy dissipation. Our ice rheology

takes multiple creep mechanisms into account, which dominate at different stress levels.

In addition to diffusion and advection of heat, we include the temperature dependence

of material properties and a simplified representation of surface crevassing assuming a

temporally steady state of stress and flow velocity. To estimate melt rates based on latent

heat, we limit temperature to the melting point and estimate melt rates based on latent

heat. As detailed in Appendix A, we solve the governing equations numerically using finite

differences for a Cartesian grid with three refinement levels after carefully benchmarking

our computational technique against approximate analytical results.

Our model is intended as a representation of the Ross Ice Streams. Despite the general

scope of the model, we chose the southern margin of Whillans Ice Stream B2, commonly

referred to as Dragon margin (Figure 1), as a specific test case for our study. Dragon

margin is located near research camps and skiways and has been studied extensively.

The two most important data sets for our purposes are detailed observations of surface

velocities [*Echelmeyer et al.*, 1994; *Echelmeyer and Harrison*, 1999] and temperature

measurements from nine boreholes distributed across Dragon margin [*Harrison et al.*,

1998] (Figure. 2). In addition, *Jackson and Kamb* [1997] measured the enhancement factor

at Dragon margin to fit the observed rheology with the standard parametrization of Glen's

106 Law, and *Clarke et al.* [2000] provided valuable insights into the complex deformational

107 history of the area over the last few hundred years.

2. Model setup

108   We consider a slab of ice flowing in the downstream direction x (Figure 3). The height

109 coordinate, z, is taken positive upward from the base of the ice. In the transverse direction,

110 the ice stream extends from the left boundary of the domain to its center $(-W/2 \leq y \leq 0)$

111 and the ridge from the center to the right boundary of the domain $(0 \leq y \leq W/2)$. The

112 left boundary of our modeling domain thus coincides with the middle of the stream, and

113 the origin of our coordinate system $(y = 0, z = 0)$ represents the transition point from

114 slipping to locking at the bed, indicated as a black dot in Figure 3. We do not explicitly

115 model the process that would lead to such a transition. We distinguish the locked-to-

116 sliding transition point from the shear margin itself, which constitutes the ice column at

117 the lateral boundary of the stream where the surface velocity of ice increases rapidly over

118 a few kilometers. We assume negligible variation of ice-sheet thickness in the transverse

119 direction (along the y axis) and neglect topography at the bed such that the ice surface

120 is parallel to the bed. We also neglect downstream variation of ice properties and flow

121 speed u, which reduces our model to two dimensions, and assume a lithostatic pressure

122 field. All notations used in this paper are summarized in Table 1 at the end of the paper.

2.1. Mechanical model

123   The only free variable of our mechanical model is the downstream velocity $u(y, z)$, which

124 reduces the conservation of momentum (or static equilibrium in this case) to

$$\frac{\partial}{\partial y}\left(\mu\frac{\partial u}{\partial y}\right) + \frac{\partial}{\partial z}\left(\mu\frac{\partial u}{\partial z}\right) + \rho g \sin\alpha = 0 \tag{1}$$

125

where ρ is the ice density, g is the acceleration due to gravity, α is the inclination angle of

the ice, and μ is the temperature- and strain-rate-dependent effective dynamic viscosity.

Accordingly, we assume that the strain-rate tensor $\dot{\boldsymbol{\epsilon}}$ and the deviatoric stress tensor $\boldsymbol{\tau}$

have only two non-negligible components, the shear strain rates and shear stresses in

horizontal ($\dot{\epsilon}_{xy}$ and τ_{xy}) and vertical ($\dot{\epsilon}_{xz}$ and τ_{xz}) directions on a face where x is constant.

Note that by reducing our analysis to anti-plane deformation as in eq. 1, we inevitably

neglect small components of in-plane deformation that must accompany the marginal

melting and drainage that we later infer.

The stream-ridge system in Figure 3 is underlain everywhere by a thick layer of glacial

till. Underneath the ice stream, the till is failing in shear, which justifies equating the

basal shear stress, τ_{base}, underneath the ice stream with the yield stress. In the interest of

simplicity, we assume that the basal stress is constant. Underneath the ridge, we assume

that the shear stress at the ice-till interface does not exceed the yield stress, implying that

failure and sliding do not occur. The full details that explain locking are yet to be fully

understood. The appropriate boundary conditions at the bed are then

$$\tau_{xz} = \tau_{base} \quad \text{at} \quad z = 0, \, y \leq 0 \tag{2}$$

$$u = 0 \quad \text{at} \quad z = 0, \, y > 0 \,. \tag{3}$$

The ice surface is assumed to be stress free. On the sides of the modeling domain, we

use symmetric boundary conditions, implying an infinite juxtaposition of ice streams and

ridges. Later, we estimate τ_{base} to best match measured surface flow rates and borehole

temperature profiles.

The boundary conditions defined in eqs. 2 and 3 imply a stress singularity at the bed $(z = 0, y = 0)$. This singularity is caused by the assumed till rheology, which posits that till transitions from locking to yielding almost discontinuously. The extreme stress concentration at the locked-to-sliding transition in the shear margin has important ramifications for understanding ice-stream dynamics because it implies an inherent instability in which ice streams that experience slight perturbations might be prone to instability [*Jacobson and Raymond*, 1998]. That being said, it is possible that the singularity would be smoothed out by melting, as discussed later in detail, or a Dugdale-Barenblatt cohesive zone.

2.2. Ice rheology

There is no single mechanism that captures how ice deforms over a wide range of stresses [*Cuffey and Paterson*, 2010]. For our modeling domain, which encompasses both high and low stress conditions, we approximate the rheology of ice as a combination of diffusional creep $\dot{\boldsymbol{\epsilon}}_D$ and Glen's Law $\dot{\boldsymbol{\epsilon}}_G$

$$\dot{\boldsymbol{\epsilon}} = \dot{\boldsymbol{\epsilon}}_D + \dot{\boldsymbol{\epsilon}}_G \,. \tag{4}$$

Diffusional creep

$$(\dot{\epsilon}_D)_{ij} = \frac{42\Omega}{k_B T d^2} B \exp\left(-\frac{Q}{RT}\right) \tau_{ij} \tag{5}$$

dominates the deformational behavior of ice at low stresses, and Glen's Law

$$(\dot{\epsilon}_G)_{ij} = AE \exp\left[-\frac{Q}{R}\left(\frac{1}{T_h} - \frac{1}{T^*}\right)\right] \tau_E^2 \tau_{ij} \tag{6}$$

dominates at intermediate to high stresses, where τ_E is the effective shear stress defined by the second invariant of the deviatoric stress tensor, in our case $\tau_E^2 = \tau_{xy}^2 + \tau_{xz}^2$, and $\dot{\epsilon}_E$ is the effective tensorial deviatoric strain rate, in our case $\dot{\epsilon}_E^2 = \dot{\epsilon}_{xy}^2 + \dot{\epsilon}_{xz}^2$.

169   The parameters specifying diffusional creep in eq.   5 are the molecular volume

170   $\Omega = 3.27\,10^{-29}\,\text{m}^3$, the Boltzmann constant $k_B = 1.38\,10^{-23}\,\text{m}^2\,\text{kg}\,\text{s}^{-2}\,\text{K}^{-1}$, the grain

171   size $d = 1\text{-}10\,\text{mm}$, the exponential prefactor $B = 9.1\,10^{-4}\,\text{m}^2\,\text{s}^{-1}$, the activation energy

172   $Q = 59.4\,\text{kJ}\,\text{mol}^{-1}$ and the gas constant $R = 8.314\,\text{J}\,\text{K}^{-1}\text{mol}^{-1}$ [*Frost and Ashby*, 1982].

173   For Glen's Law (eq. 6), we follow *Cuffey and Paterson* [2010] in using the pre-exponential

174   constant $A = 3.5\,10^{-25}\,\text{s}^{-1}\text{Pa}^{-3}$, the temperature adjusted for the pressure effect on the

175   melting point depression $T_h = T + p_0 P$ with $p_0 = 7 \times 10^{-8}\,\text{K}\,\text{Pa}^{-1}$ and T in K and the

176   activation energy $Q = 60\,\text{kJ}\,\text{mol}^{-1}$ for $T_h < T^*$ and $Q = 115\,\text{kJ}\,\text{mol}^{-1}$ for $T_h > T^*$ where

177   $T^* = 263.15\,\text{K} = -10°\text{C}$. The sum of the coefficients of τ_{ij} in eqs. 5 and 6 defines $1/(2\mu)$.

178   The rheological parameter that is most difficult to constrain is the enhancement factor.

179   Enhancement is not a physical variable by itself but rather represents effects of grain

180   size, impurities, fabrics and possibly other variables [*Cuffey and Paterson*, 2010]. As

181   a consequence, estimates for enhancement vary widely. For the specific case of Dragon

182   margin, *Jackson and Kamb* [1997] determined enhancement factors between $E \approx 1.12$

183   and $E \approx 2.55$ for different ice specimens retrieved from Dragon margin. Because of the

184   significant ambiguity introduced into our model results even by this moderate variation,

185   we set $E = 1$ for most of our computations to allow for easier comparisons. We discuss

186   the ramifications of varying enhancement in Section 4.

2.3. Thermal model

187   Our thermal model captures the effect of both diffusion and advection of heat. In

188   addition, we cap temperature at the melting point to estimate melt production based on

189   latent heat and include the effect of cold surface air pooling in crevasses [*Harrison et al.*,

190   1998]. For a spatially-variable thermal conductivity k, the steady-state temperature field

is thus given by

$$\frac{\partial}{\partial y}\left(k\frac{\partial T}{\partial y}\right) + \frac{\partial}{\partial z}\left(k\frac{\partial T}{\partial z}\right) - \rho c\left(v\frac{\partial T}{\partial y} + w\frac{\partial T}{\partial z}\right) + 2\tau_E\dot{\epsilon}_E - L\dot{m} = 0\,, \tag{7}$$

where v and w are the lateral and vertical advection speeds, respectively, c is the specific heat of ice, τ_E is the effective shear stress, $\dot{\epsilon}_E$ is the effective tensorial shear strain rate, L is the latent heat of ice per unit mass and $\dot{m}$ is the mass melting per unit time and unit volume. The thermal conductivity k and specific heat c vary with temperature as summarized in *Cuffey and Paterson* [2010]:

$$k(T) = k_1\,\exp(-k_2 \times 10^{-3}\,T) \tag{8}$$

$$c(T) = c_1 + c_2\,T\,, \tag{9}$$

where T is in Kelvin and the forefactors are $k_1 = 9.828\,\mathrm{W\,m^{-1}\,K^{-1}}$, $k_2 = 5.7\,\mathrm{K^{-1}}$, $c_1 = 152.5\,\mathrm{J\,kg^{-1}\,K^{-1}}$ and $c_2 = 7.122\,\mathrm{J\,kg^{-1}\,K^{-2}}$, respectively.

To compute the melt rate per unit volume $\dot{m}$ in eq. 7, we assume that shear heating in the temperate zone is absorbed as latent heat. This assumption implies that the temperature in the temperate zone is capped at the melting point, which allows us to reduce eq. 7 to the following non-linear Poisson problem:

$$\frac{\partial}{\partial y}\left(k\frac{\partial T}{\partial y}\right) + \frac{\partial}{\partial z}\left(k\frac{\partial T}{\partial z}\right) - \rho c\left(v\frac{\partial T}{\partial y} + w\frac{\partial T}{\partial z}\right) + [1 - H(T - T_m)]\,2\tau_E\dot{\epsilon}_E = 0\,, \tag{10}$$

where $H(T - T_m)$ denotes the Heaviside function. $H(T - T_m)$ is one in the temperate zone and zero outside such that $L\dot{m}$ is non-zero only in the temperate zone where it equals the shear heating $2\tau_E\dot{\epsilon}_E$.

The mechanical model set up in Section 2.1 solves only for the downstream velocity u. To include the horizontal and vertical velocities into our thermal model, we constrain

213 the functional forms for both v and w a priori, assuming that the associated strain rates,

214 stresses and work rates are negligible. Considering horizontal and vertical velocities in the

215 thermal but not the mechanical model is, of course, strictly inconsistent. This inaccuracy

216 is warranted by the potentially important effect that the advection of cold ice into the

217 shear margin is likely to have on deformation-induced melting [*Jacobson and Raymond*,

218 1998]. In the mechanical model, however, the strain rates associated with the horizontal

219 and vertical velocities are two orders of magnitude smaller than the anti-plane rates,

220 implying that the strain rate components in these directions can be neglected in $\dot{\epsilon}_E$ of the

221 creep law and the equilibrium equation.

222   For the vertical advection component we assume that w varies linearly with depth

223 [*Zotikov*, 1986]

$$w(y, z) = -a\frac{z}{H}\,, \tag{11}$$

225 where a is the surface accumulation rate of ice in m/yr, and a uniform contribution to

226 w equal to the melt rate at the bed of the ice sheet is neglected. Eq. 11 implies that

227 accumulation of ice at the surface is compensated by downslope stretching of ice and that

228 basal melting or freeze-on are negligible [*Zotikov*, 1986], which is probably not strictly

229 true in the shear margin.

230   Several studies have suggested that the position of Dragon margin has shifted in the

231 past and may even be shifting currently with speeds on the order of $1 - 10$ m/yr [*Harrison*

232 *et al.*, 1998; *Echelmeyer and Harrison*, 1999] to potentially ≈ 100 m/yr [*Bindschadler*

233 *and Vornberger*, 1998; *Clarke et al.*, 2000]. The simplest way to include ongoing margin

234 migration at a constant rate into our ice-stream model is through the influx of cold ice

235 from the ridge based on the rationale that in a coordinate system moving with the margin,

outward expansion of the stream is equivalent to influx of cold ice from the ridge (as also

argued in *Schoof* [2012]). To be consistent with the zero-slip boundary condition at the

bed underneath the ridge, we impose

$$v(y, z) = v_0 \left[1 - \left(\frac{H - z}{H} \right)^4 \right] \tag{12}$$

instead of a depth-independent horizontal velocity as suggested by *MacAyeal* [1989]. We

performed computations with both expressions for the horizontal velocity component and

found only slight differences.

Similar to the mechanical model, we use a symmetric boundary condition on the sides

of the domain. On the top, we specify the surface temperature of ice (see Section 2.5).

Underneath the stream, we assume that the bed is at the melting point as supported by

observations (e.g., *Engelhardt et al.* [1990]). Underneath the ridge, we do not specify a

priori whether the bed is temperate or not. Instead, we adjust the geothermal heat flux G

directly beneath the ice sheet such that the bed reaches a temperature of $-5°$C at large

distances from the margin in agreement with observations (e.g., *Rose* [1979]). Depending

on the computation, this condition typically requires geothermal heat fluxes on the order

of $G = 48$-$85\,\mathrm{mW/m^2}$. We assume the same geothermal heat flux underneath the stream.

The assumption of a finite geothermal heat flux underneath the ice stream has no effect on

the solution for the downstream velocity and temperature because the additional heating

does not raise the base temperature above the melting point. It does, however, affect

the total meltwater generation associated with both the geothermal heat flux and the

frictional heating at the base of the ice stream (see Section 2.4).

2.4. Meltwater production

Despite the fact that our mechanical model (Section 2.1) entails a stress singularity, it is an integrable singularity from the standpoint of both force equilibrium and heat balance, which allows us to use the dissipation in the temperate zone to obtain an estimate for the melt rate per unit volume (see Section 2.3). In 2D, the mass balance for the meltwater produced in the temperate zone is

$$\frac{\partial q_y}{\partial y} + \frac{\partial q_z}{\partial z} = -\frac{2\tau_E \dot{\epsilon}_E}{L\rho_w} \, , \tag{13}$$

where q_y and q_z represent the meltwater flux in horizontal and vertical directions, respectively, and ρ_w is the density of water.

For simplicity, we neglect meltwater flux in the horizontal direction, $q_y = 0$, noting that we have previously assumed a hydrostatic pressure in our mechanical model (Section 2.1). We then integrate eq. 13 numerically to obtain the basal meltwater flux due to shear heating in the temperate zone very simply as

$$q_{temp} = -\int_0^{H_m} \frac{\dot{m}}{\rho_w} \mathrm{dz} = -\int_0^{H_m} \frac{2\tau_E \dot{\epsilon}_E}{L\rho_w} \mathrm{dz} \, , \tag{14}$$

where H_m indicates the height of the temperate zone measured from the bed upwards. The possibility of a finite meltwater flux in vertical direction raises the question whether the permeability entailed by the flux we compute is consistent with measurements. Assuming that meltwater percolation occurs through Darcy's law [*Lliboutry*, 1996] and that the water pressure in veins equals the ice overburden pressure, $\mathrm{d}p/\mathrm{d}z = -\rho g$, we estimate the permeability of the temperate ice as [*Perol and Rice*, 2011]

$$\kappa = \frac{q_{temp}\,\mu_w}{(\rho - \rho_w)g} \, . \tag{15}$$

277 The meltwater fluxes we later infer imply temperate-ice permeabilities on the order of

278 $10^{-16}\,\mathrm{m}^2$, which agrees with experimental results (e.g., *Jordan and Stark* [2001]).

279   Permeabilities in the estimated range are sufficiently high to allow for meltwater per-

280 colation to the base over the time scales considered here, and we will thus assume for the

281 remainder of the paper that all of the water created in the temperate zone rains down to

282 the bed. In addition to melt production from shear heating, frictional heat dissipation at

283 the bed and the difference between heat in- and out-flux may contribute to the meltwater

284 flux, yielding

$$q_{base} = q_{temp} + \frac{1}{L\rho_w}\left[u(y,0)\tau_{base} + G - k\frac{\partial T}{\partial z}\right].\tag{16}$$

2.5. Surface crevassing

286   The crevassed zone at Dragon margin consists of an approximately 2 km-wide zone

287 of intense, chaotic crevassing [*Vornberger and Whillans*, 1990; *Harrison et al.*, 1998;

288 *Echelmeyer and Harrison*, 1999]. On the ridge side of the margin, the chaotic crevasses

289 transition to large arcuate crevasses and on the stream-side to somewhat organized and

290 widely spaced crevasses that tend upstream [*Harrison et al.*, 1998; *Echelmeyer and Har-*

291 *rison*, 1999]. The crevasses are thought to extend about 30 m into the ice [*Harrison et al.*,

292 1998]. The location of the crevassed zone and the positions of the nine boreholes for which

293 *Harrison et al.* [1998] reported temperature measurements are reproduced in Figures 1A

294 and B. *Harrison et al.* [1998] also indicate the transverse derivatives of the surface veloc-

295 ities at the three boreholes, "Dragon Pad", "Lost Love" and "Chaos" (Figure 2), which

296 indicates that borehole "Dragon Pad" is located closest to the locked-to-sliding transition

297 but on the ridge side at approximately $y = 200$ in our modeling domain (Figure 3).

298   We represent the zone of chaotic crevassing as a 2 km-wide rectangular area in our y, z-

299 plane that extends from the surface 30 m into the ice. We assume that the dense spacing of

300 open crevasses lowers the effective viscosity in this area by an order of magnitude as com-

301 pared to uncrevassed ice (i.e., from μ to $\mu/10$). We refer to the drop in effective viscosity

302 as the mechanical-weakening factor. While this choice is somewhat arbitrary, we verified

303 that the results are not sensitive to the assumed value, mostly because the crevassed zone

304 is relatively shallow. To capture the zones of arcuate and upstream crevassing on the ridge

305 and stream sides of the chaotic zone, we gradually lower the effective viscosity unaffected

306 by crevassing to the mechanically weakened effective viscosity representative of chaotic

307 crevassing over 400 m on both the stream and the ridge sides. We include the effect of

308 cool winter air pooling in the crevasses by enforcing a surface temperature of $-34°C$ in

309 the crevassed zone, which gradually increases to $-26°C$ in the uncrevassed ice.

310   There is no doubt that the representation of surface crevassing considered here is ex-

311 tremely simplified. A more complete model would allow the crevassed zone to evolve

312 self-consistently instead of specifying its extent a priori. Nonetheless, we argue that the

313 approach we have chosen here provides a reasonable first step for considering crevassing in

314 the context of a steady-state model and is preferable to not including crevassing at all be-

315 cause it allows us to compare computed temperature fields to the borehole measurements

316 from *Harrison et al.* [1998].

3. Results

317   To gain a better understanding of the different effects that contribute to the thermome-

318 chanics of ice streams, we start by reducing our model to its bare minimum. In its most

319 simplistic form, the model is reminiscent of models that are amenable to analytical solution

like *Schoof* [2004]. Then, we add in one term after another, gradually obtaining a more

realistic representation of the behavior of a stream-ridge system. The sequence of effects

that we consider is as follows: First, we investigate the ramifications of a temperature-

dependent creep rheology. Second, we consider the ramifications of vertical and horizontal

advection of cold ice into the margin. Third, we take into account crevasses along the

surface expression of the margin. To quantify the explanatory potential of this sequence

of approximations, we attempt to reproduce the surface velocities measured for Dragon

margin [*Echelmeyer and Harrison*, 1999] at each step and compare the respective fits.

We limit the ambiguity introduced into our model by a large number of parameters by

varying only the basal stress to fit observed surface velocities in Sections 3.1 and 3.2 while

all other model parameters are fixed. We find that the best-fitting basal stresses depend

sensitively on the model assumptions, which highlights the strongly nonlinear nature of

the thermomechanical behavior of ice streams. When comparing our computations to

the temperature data by *Harrison et al.* [1998] in Section 3.3, we additionally adjust the

accumulation rate and the speed of margin migration because we are unable to obtain a

satisfactory fit by focusing exclusively on basal stress.

3.1. The importance of a temperature-dependent rheology

The most significant assumption in analytical models of ice-stream dynamics is prob-

ably the usage of a simplified rheology, such as a constant Newtonian viscosity [*Schoof*,

2004, 2012] or a temperature-independent power-law rheology. In this section, we quantify

the ramifications of using a simplified rheology by comparing our model predictions to

the surface velocities at Dragon margin observed by *Echelmeyer and Harrison* [1999]. All

computations in this section are based on the reduced thermal model

$$\frac{\partial}{\partial y}\left(k\frac{\partial T}{\partial y}\right) + \frac{\partial}{\partial z}\left(k\frac{\partial T}{\partial z}\right) + \left[1 - H(T - T_m)\right]2\tau_E\dot{\epsilon}_E = 0\,, \tag{17}$$

which neglects the advective terms and the effect of surface crevassing as compared to the

full thermal model defined in Section 2.3. The latter two effects are discussed in detail in

the subsequent sections.

In Figure 4, we compare the temperate zones and predicted surface velocities for three

different rheologies. We adjust the basal stress to reproduce the surface velocity in the

center of the stream exactly, and then we align the computed velocity profile to minimize

the mean square error in the shear margin. The computation on top (Figures 4A1 and

B1) is based on a constant Newtonian rheology of $\mu = 10^{14}\,\mathrm{Pa\,s}$, which clearly gives the

worst fit to observational data. The computation in the middle (Figures 4A2 and B2)

takes the strain-rate dependence of the rheology into account but neglects the temperature

dependence. While this scenario is clearly more realistic than the Newtonian case, the

width of the shear margin is overestimated by approximately a factor of two. Considering

a realistic rheology that takes both the strain-rate and the temperature dependence into

account improves the fit to observations dramatically (Figures 4A3 and B3). The extent of

the temperate zone in the last computation (Figures 4A3 and B3) is roughly comparable

to the observations by *Clarke et al.* [2000].

Figure 5 demonstrates why the temperature dependence of the ice rheology is such

an important effect. It shows the spatial variation in shear heating in the vicinity of

the singularity for the strain-rate dependent rheologies (Figures 4A2, B2 and A3, B3).

Both cases show a pronounced peak in shear heating at the slip singularity. When taking

363   temperature into account, we find a second local maximum in shear heating at the ice

364   surface above the singularity. The reason is that the ice is coldest on the surface, which

365   translates into higher effective viscosity and higher shear heating than in the ice below.

366   We conclude that the width of the high-strain region at the margin is controlled primarily

367   by differences in the temperature of ice and thereby in its effective viscosity. To reproduce

368   the rapid increase in surface speeds observed at Dragon margin [*Echelmeyer and Harrison*,

369   1999], the ice in the margin has to be significantly warmer and thus weaker than the ice

370   outside.

3.2. The effect of advection

371   The computations in Figure 4 indicate that a significant portion of the ice in Dragon

372   margin is temperate. However, both models may overestimate the volume of temperate

373   ice because they do not consider the effect of cold ice being advected into the margin both

374   from the surface and from the ridge. To better isolate the effect of horizontal as opposed

375   to vertical advection, we study them through separate simulations. The thermal model

376   we consider is thus eq. 10 with $v = 0$ and $w = 0$, respectively.

377   To test the effect of vertical advection only, we first assume the same basal stress ($\tau_{base} =$

378    $4.07\,\mathrm{kPa}$) as in Figures 4A3 and B3. We add vertical advection assuming an accumulation

379   of $a = 0.1\,\mathrm{m/yr}$, which is on the low end of the estimated accumulation of $0.1 - 0.2\,\mathrm{m/yr}$

380   for Antarctica [*Giovinetto and Zwally*, 2000; *Joughin et al.*, 2002; *Spikes et al.*, 2004]. We

381   find that the temperate zone vanishes almost entirely. The associated surface velocities

382   in the ice stream, however, are now much lower than observations suggest [*Echelmeyer*

383   *and Harrison*, 1999]. The reason is that by cooling the margin, vertical advection makes

384   the margin stronger, and a strong margin provides more resistance against gravity than

385 a weak one. To reproduce the observed surface velocities, we have to lower the assumed

386 basal stress underneath the ice stream to $\tau_{base} \approx 3.17\,\text{kPa}$. Figures 6A1 and B1 show

387 the resulting temperature field and surface velocities. Interestingly, the extent of the

388 temperate zone is now comparable to that in Figure 4A3. We thus conclude that the main

389 effect of vertical advection, if we insist that the surface deformation data be matched, is

390 to slightly shift the force balance between the resistance to flow provided by the shear

391 margin as compared to basal friction. The extent of the temperate zone in the margin

392 changes only slightly after accounting for the different basal stress required to balance

393 gravity. We have verified that this conclusion remains valid for accumulation rates of

394 $a = 0.2\,\text{m/yr}$.

395   Observations suggest that Dragon margin is currently moving outwards at a constant

396 speed of $7.3\,\text{m/yr}$ [*Harrison et al.*, 1998], which is equivalent to including horizontal ad-

397 vection at $-7.3\,\text{m/yr}$, and possibly more rapidly [*Echelmeyer and Harrison*, 1999]. The

398 effect of including horizontal advection at $-7.3\,\text{m/yr}$ is shown in Figures 6A2 and B2. As

399 a consequence of the lateral influx of cold ice from the ridge, the temperate zone vanishes

400 entirely, and it becomes impossible to reproduce the rapid increase in the observed surface

401 speed of ice in our computations. The finding that horizontal advection on the order of

402 m/yr precludes the formation of a temperate zone is consistent with the previous study by

403 *Jacobson and Raymond* [1998]. Our simulations indicate that horizontal advection with

404 speeds on the order of $0.1\,\text{m/yr}$ are associated with finite temperate zones, albeit smaller

405 ones than in the absence of a horizontal influx of cold ice.

406   Our inability to reproduce observed surface velocities for the estimated migration speeds

407 is clearly an important caveat. We argue that the main problem is that our simplified

representation of horizontal advection does not adequately represent the physics of margin migration. The two most important concerns are: First, it is highly questionable that margin migration as rapid as several m/yr can be treated through a steady-state model. Indeed, the evidence in favor of migration of Dragon margin comes primarily from surface lineations and subsurface diffractors that indicate a complex deformational history [*Harrison et al.*, 1998; *Echelmeyer and Harrison*, 1999; *Clarke et al.*, 2000] and both inward and outward migration of the margin [*Clarke et al.*, 2000]. The observational evidence thus suggest that the system has not reached a steady state. Second, Dragon margin is located close to the confluence between Ice Streams B1 and B2. The interaction between the two streams and the interjacent Unicorn ridge may be an important factor to consider in modeling the evolution of the system. An example of observational evidence that supports a non-trivial geometric connection between the two branches of Whillans Ice Stream is a hook-shaped surface lineation called "Fishhook", which connects the two streams and correlates with several near-surface strain features [*Clarke et al.*, 2000].

Nonetheless, the simulations including horizontal advection lend additional support to our previous conclusion that Dragon margin is at least partially temperate. Our computations show that only temperate ice is weak enough to concentrate strain to the degree necessary for the surface speed to increase from approximately zero to its maximum value over as little as 8 km. Cold ice as predicted in Figures 6A2 and B2 is more rigid than temperate ice and is consequently associated with a much wider margin than observed. The finding that Dragon margin is likely temperate over a significant portion of its thickness is consistent with *Perol and Rice* [2011]. Albeit not including horizontal advection, they predicted temperate zones in the shear margins of the active Siple-Coast Ice Streams

431 using a 1D heat-transfer model in conjunction with the shear-strain rates measured by

432 *Joughin et al.* [2002] to constrain shear heating. In fact, the size of the temperate zone

433 estimate here for Dragon margin and the results by Perol and Rice match moderately well

434 (Figure 7).

3.3. The ramifications of surface crevassing

435 The ice streams of West Antarctica were first identified by radar detection of their

436 crevassed margins [*Rose*, 1979], which highlights that intense surface crevassing is a char-

437 acteristic feature of the Ross Ice Streams. This observation raises the question of how

438 surface crevasses affect the thermomechanics of ice-stream margins. Within the framework

439 of our model, surface crevassing has two competing effects: On the one hand, crevasses

440 lower the creep resistance of the ice because of the void space they introduce into the ice.

441 We refer to this effect as mechanical weakening. On the other hand, crevasses lower the

442 temperature in the ice through cool winter air pooling in the crevasses [*Harrison et al.*,

443 1998] thus increasing the creep resistance. We call this effect thermal strengthening.

444 While we are able to reproduce the velocity data for Dragon margin [*Echelmeyer and*

445 *Harrison*, 1999] with a wide range of modeling parameters, compatibility with temperature

446 measurements [*Harrison et al.*, 1998] poses more constraints. Figures 8 and 9 illustrate

447 a computation that attempts to match both data sets simultaneously. To facilitate the

448 comparison with our simulations, we briefly summarize four key observations by *Harrison*

449 *et al.* [1998]. In the interest of consistency with the rest of this manuscript, we continue to

450 use "depth" to describe distance from the bed despite the fact that "depth" in boreholes

451 is typically measured from the surface. First, the temperature for the two boreholes in

452 the ridge, named "OutB" and "Stage" (see Figure 1 for approximate borehole locations),

₄₅₃ is approximately constant at $-26°$C over the depth range measured (Figure 8). Second,

₄₅₄ out of the nine boreholes, the boreholes "Remote", "Intermediate" and "Pad" exhibit

₄₅₅ the warmest temperature at depth ($-22°$C at a depth of approximately 700 m) with

₄₅₆ "Intermediate" being slightly cooler than the other two. Third, borehole "UpB," located

₄₅₇ well into the stream, is slightly cooler yet ($-25°$C at a depth of approximately 700 m, see

₄₅₈ Figure 8). Fourth, the $-26°$C contour extends from borehole "Dragon Pad" to borehole

₄₅₉ "Intermediate" and attains the largest depths (≈ 830 m) at boreholes "Lost Love" and

₄₆₀ "Chaos" (Figure 9).

₄₆₁   Supposing that the temperatures measured by *Harrison et al.* [1998] resemble a steady

₄₆₂ state, these four observations translate into the following constraints for our modeling.

₄₆₃ First, the finding that the boreholes in the ridge maintain a typical surface temperature of

₄₆₄ $-26°$C over a 300 m depth interval suggests high rates of vertical advection. High vertical

₄₆₅ advection in turn implies high accumulations on the order of $a = 0.20 - 0.24$ m/yr, which

₄₆₆ is reasonable for Antarctica [*Giovinetto and Zwally*, 2000; *Spikes et al.*, 2004]. Second, the

₄₆₇ relatively warm temperatures measured for "Remote", "Intermediate" and "Pad" points

₄₆₈ to internal heating at these locations. The offset between the locations of highest strain

₄₆₉ rate and highest internal heating may indicate horizontal advection probably relating to

₄₇₀ margin migration [*Harrison et al.*, 1998; *Echelmeyer and Harrison*, 1999]. Third, the

₄₇₁ comparatively cooler temperatures at "UpB" are consistent with a localized heat source

₄₇₂ close to "Remote", "Intermediate" and "Pad" that does not extend far into the stream.

₄₇₃ Fourth, we take the $-26°$C contour as a proxy for the extent and location of the crevassed

₄₇₄ zone at Dragon margin, which stretches from "Dragon Pad" to "Intermediate".

475   Figure 8A shows the computed temperature in our modeling domain. The cooling effect

476 of crevassing depresses the temperature notably in the vicinity of the shear margin. We

477 also compare computed and measured temperatures at a depth of 700 m for the three

478 boreholes that are located far from the margin. The temperatures we estimate are $1 - 2°$

479 higher than the measured values. The agreement with surface velocities (Figure 8B) is

480 slightly less satisfactory than in previous simulations (e.g., Figures 4B3 and 6B1). While

481 it is certainly possible to improve the agreement with surface velocities, doing so comes

482 at the cost of deteriorating the consistency with available temperature data. Figure 9

483 compares the computed and measured temperatures for the boreholes in the vicinity

484 of the shear margin at a depth of 700 m for the computation shown in Figure 8. We

485 successfully reproduce the extent and approximate depths of the $-26°C$ contour from

486 *Harrison et al.* [1998], highlighted on the boreholes "Dragon Pad" to "Intermediate" as

487 short horizontal dashes. Our computations are also consistent with the observation that

488 the three leftmost boreholes are warmest and that the borehole "Intermediate" is colder

489 than its two neighboring boreholes. We suggest that the relatively warmer temperatures

490 at these three boreholes could result from their proximity to a temperate zone instead

491 of non-steady state effects as argued in *Harrison et al.* [1998]. Despite being able to

492 reproduce these key features, the temperatures we compute are systematically too high

493 by $1 - 6°C$ with the highest errors occurring at the boreholes closest to the margin (i.e.,

494 "Dragon Pad", "Lost Love" and "Chaos").

495   Figure 10 summarizes the relationship between the average absolute errors in reproduc-

496 ing the observational data and the properties of the temperate zones for various speeds

497 of horizontal advection v_0. The speed of horizontal advection is the most consequential

498 parameter when reproducing both data sets simultaneously because it has a strong effect

499 on the position and extent of the temperate zone and thereby on the surface velocities.

500 The speed of vertical advection, in comparison, is reasonably well constrained by fitting

501 the temperature measurements in boreholes "OutB" and "Stage" (Figure 8A) and does

502 not affect the shear margin as sensitively (see also the discussion in Section 3.2). Figure 10

503 highlights that the maximum height and the shape of the temperate zones are highly de-

504 pendent on the assumed speed of horizontal advection. It is also evident from Figure 10

505 that large temperate zones entail more realistic surface velocities, while small temperate

506 zones produce more realistic temperatures. We argue that horizontal advection on the

507 order of $v_0 = -0.3$ to -0.35 m/yr probably provide a reasonable compromise (Figures 8

508 and 9 show the case where $v_0 = -0.35$ m/yr). Increasing the speed of horizontal advection

509 beyond $v_0 \approx -0.35$ m/yr deteriorates the fit to observed surface velocities notably (similar

510 to Figure 6B2) while improving the match to measured temperatures only minimally.

511   The temperate zones for horizontal-advection speeds between $v_0 = -0.3$ and -0.35 m/yr

512 reach a maximum height of $120 - 160$ m. In the vicinity of the locked-to-sliding transition

513 point, the height of the temperate zone has a second maximum of approximately 80 m.

514 The widths of the temperate zones, which we define as the maximum width range over

515 which ice is temperate not only at the bed but at a finite depth, are approximately 2.2

516 and 2.3 km. We obtain the total meltwater production by integrating the basal meltwater

517 flux over the temperate zone, which extends from about $y = -16.94$ km to $y = 512$ m for

518 $v_0 = -0.30$ m/yr and from $y = -19.30$ km to $y = 413$ m for $v_0 = -0.35$ m/yr, is 26.5 and

519 25 m^3 per year and per meter in downstream direction, respectively. Increasing the rate

520 of outward margin migration shifts the temperate zone further into the stream, depresses

the maximum depth to which temperate ice extends and decreases the total meltwater production (Figure 10).

When weighing how to prioritize the two data sets, it is important to keep in mind that a steady-state approach to modeling the temperatures throughout Dragon margin is in itself highly questionable (see also Section 3.2). A simple scaling analysis shows that the time it takes for the full ice thickness to reach steady state, $t = H^2/\alpha_{th}$, is approximately 10^4 years. In contrast, *Harrison et al.* [1998] estimated that the residence time of ice in Dragon margin is approximately a half century. It is thus clear that the stream-ridge system can not possibly be in steady state. This insight is supported by field observations that indicate a complex deformational history dating back over the last few hundred years [*Harrison et al.*, 1998; *Echelmeyer and Harrison*, 1999; *Clarke et al.*, 2000]. Non-steady state effects should be most significant for the boreholes closest to the margin because of the rapid margin migration in recent years [*Harrison et al.*, 1998; *Echelmeyer and Harrison*, 1999]. The observation that the deviations between computed and observed temperatures are indeed highest in the shear margin lends support to the interpretation that non-steady effects are probably the main reason for the temperature mismatch between model and data.

4. Discussion

While several previous models of ice streams [*Jacobson and Raymond*, 1998; *Schoof*, 2004; *Beem et al.*, 2010; *Perol and Rice*, 2011] have raised the possibility of melting in active ice-stream margins, only *Perol and Rice* [2011] discuss the extent of a potential temperate zone in detail (see Figure 7 for a comparison with their results). In this study, we provide additional constraints on how different factors such as the assumed ice rheol-

ogy (Section 3.1), horizontal and vertical advection (Section 3.2) and surface crevassing

(Section 3.3) affect deformation-induced melting and the size of a potential temperate

zone.

While the simulations presented in Sections 3.1 and 3.2 raise the possibility that a

temperate zone may extend several hundred meters above the bed at Dragon margin, the

borehole measurements by *Harrison et al.* [1998] indicate variable but cold temperatures in

the upper $300-400\,\mathrm{m}$ of the ice. In Section 3.3 we thus attempt to fit velocity [*Echelmeyer*

and Harrison, 1999] and temperature data [*Harrison et al.*, 1998] simultaneously. We

find that the two data sets provide somewhat conflicting constraints on the size of a

potential temperate zone: While the agreement with surface velocities improves for a

large temperate zone, the agreement with temperature measurements improves for a small

temperate zone. We suggest that the computation shown in Figures 8 and 9 represents a

reasonable compromise between the two constraints. This particular computation entails

a temperate zone with a maximum height of $\approx 120\,\mathrm{m}$ and entails a meltwater production

of $25\,\mathrm{m^3/yr}$ per meter in the downstream direction (Figure 9).

As discussed in more detail in Section 3.3, it is unreasonable to expect that temper-

ature data can be reproduced exactly within the confines of a steady-state model (see

Section 3.3), particularly for a location with a complex deformational history like Dragon

margin [*Clarke et al.*, 2000]. To remedy the difficulties associated with replicating mea-

sured surface velocities without allowing for melting, *Echelmeyer et al.* [1994] and *Scambos*

et al. [1994] have chosen to adjust the enhancement factor and its spatial variability in

the model. It is certainly possible to match the surface velocity *Echelmeyer and Harrison*

[1999] and temperature [*Harrison et al.*, 1998] data for Dragon margin only by varying

enhancement in different parts of the stream-ridge system. However, we require very high

enhancement values on the order of $15 - 20$ in the shear margin to obtain a satisfactory

fit to observational data, which conflicts with the results of *Jackson and Kamb* [1997],

who determined enhancement factors between $E \approx 1.12$ and $E \approx 2.55$ for different ice

specimens retrieved from Dragon margin.

Our simulations show that it is not necessary to resort to very high enhancement factors

to reproduce rapid velocity increases in shear margins. We obtain excellent agreement

with surface velocities even when neglecting enhancement entirely. This insight is not

meant to imply that varied effects such as fabric, impurities or grain-size variations, which

are usually integrated into a single enhancement factor, are not important. Instead, we

argue that the relatively small enhancement factors measured at Dragon margin [*Jackson*

and Kamb, 1997], in combination with our simulations, suggest that enhancement effects

are probably not the whole story and that deformation-induced melting may play an

important role in the thermomechanics of ice-stream margins, as is also supported by

some observations [*Clarke et al.*, 2000; *Vogel et al.*, 2005].

5. Conclusion

In this study, we investigate the possibility of deformation-induced melting in active

shear margins. Melting and the associated presence of meltwater in ice-stream margins

might have important consequences for the dynamics of ice streams, primarily because the

yield strength of glacial till depends sensitively on porosity, which is controlled by the wa-

ter content if saturated. The position of the shear margins could thus be intricately linked

to meltwater production [*Raymond*, 1996, 2000], which remains poorly constrained. We

devise a 2D thermomechanical model of an ice stream moving over a plastic bed in steady

state. We solve our model numerically after carefully benchmarking our computational approach against an asymptotic analytic solution. In combination with previous studies [*Jacobson and Raymond*, 1998; *Schoof*, 2004; *Perol and Rice*, 2014], our simulations lend theoretical support to the hypothesis that active shear margins are partially temperate. For Dragon margin, we estimate a temperate zone with a maximum height of ~ 120 to $150\,\text{m}$ that produces approximately 25 to $26.5\,\text{m}^3$ meltwater per year and per meter in the downstream direction. This estimate for the extent of a temperate zone is roughly comparable to the height of the bottom diffractor identified by *Clarke et al.* [2000] under Unicorn ridge. Despite focusing primarily on Dragon margin, we argue that our insights may generalize to the other active Ross Ice Streams.

References

Alley, R., D. Blankenship, C. Bentley, and S. Rooney, Deformation of till beneath Ice Stream B, West Antarctica, *Nature*, *322*, 57–59, 1986.

Bamber, J. L., D. G. Vaughan, and I. Joughin, Widespread complex flow in the interior of the antarctic ice sheet, *Science*, *287*(5456), 1248–1250, 2000.

Beem, L., K. Jezek, and C. Van der Veen, Basal melt rates beneath Whillans Ice Stream, West Antarctica, *Journal of Glaciology*, *56*(198), 647–654, 2010.

Ben Amar, M., and J. Rice, Exacts results with the J-integral applied to free-boundary flows, *Journal of Fluid Mechanics*, *461*, 321–341, 2002.

Bilby, B., and J. Eshelby, Dislocations and the Theory of Fracture, in *Fracture: An Advanced Treatise: Vol. 2, Mathematical Fundamentals*, edited by H. Liebowitz, pp. 99–182, Academic Press, N.Y., 1968.

Bindschadler, R., and P. Vornberger, Changes in the west antarctic ice sheet since 1963 from declassified satellite photography, *Science*, *279*(5351), 689–692, 1998.

Briggs, W. L., V. E. Henson, and S. F. McCormick, *A Multigrid Tutorial*, vol. 72, Siam Monograph, 2000.

Cherepanov, G., Cracks in solids, *International Journal of Solids and Structures*, *4*(8), 811–831, 1968.

Clarke, T. S., C. Liu, N. E. Lord, and C. R. Bentley, Evidence for a recently abandoned shear margin adjacent to ice stream B2, Antarctica, from ice-penetrating radar measurements, *Journal of Geophysical Research*, *105*(B6), 2000.

Cuffey, K., and W. Paterson, *The Physics of Glaciers (Fourth Edition)*, ISBN 9780123694614, Elsevier, 2010.

Dreimanis, A., *Genetic classification of glacigenic deposits*, chap. Tills: their genetic terminology and classification, pp. 17–83, Balkema, Rotterdam, 1988.

Echelmeyer, K., and W. Harrison, Ongoing margin migration of ice stream b, antarctica, *Journal of Glaciology*, *45*(150), 361–369, 1999.

Echelmeyer, K., W. Harrison, C. Larsen, and J. Mitchell, The role of the margins in the dynamics of an active ice stream, *Journal of Glaciology*, *40*(136), 527–538, 1994.

Engelhardt, H., N. Humphrey, B. Kamb, and M. Fahnestock, Physical conditions at the base of a fast moving antarctic ice stream, *Science*, *248*, 57–59, 1990.

Fahnestock, M., T. Scambos, R. Bindschadler, and G. Kvaran, A millennium of variable ice flow recorded by the ross ice shelf, antarctica, *J. Glaciol.*, *46*(155), 652–664, 2000.

Frost, H., and M. Ashby, Deformation mechanism maps: the plasticity and creep of metals and ceramics, 1982.

Giovinetto, M. B., and H. J. Zwally, Spatial distribution of net surface accumulation on the antarctic ice sheet, *Annals of Glaciology*, *31*(1), 171–178, 2000.

Goldman, N. L., and J. W. Hutchinson, Fully plastic crack problems: The center-cracked strip under plane strain, *International Journal of Solids and Structures*, *11*(5), 575–591, 1975.

Harrison, W., K. A. Echelmeyer, and C. Larsen, Measurement of temperature in a margin of Ice Stream B, Antarctica : implications for margin migration and lateral drag, *Journal of Glaciology*, *44*(148), 1998.

Iverson, N., T. Hooyer, and R. Baker, Ring-shear studies of till deforrnation: Coulotnb-plastic behavior and distributed strain in glacier beds, *Journal of Glaciology*, *44*(148), 634–642, 1998.

Jackson, M., and B. Kamb, The marginal shear stress of Ice Stream B, West Antarctica, *Journal of Glaciology*, *43*(145), 415–426, 1997.

Jacobel, R., T. Scambos, C. Raymond, and A. Gades, Changes in the configuration of ice stream flow from the west antarctic ice sheet, *Journal of Geophysical Research*, *101*(B3), 5499–5504, 1996.

Jacobel, R., T. Scambos, N. Nereson, and C. Raymond, Changes in the margin of ice stream c, antarctica, *Journal of Glaciology*, *46*(152), 102–110, 2000.

Jacobson, H., and C. Raymond, Thermal effects on the location of ice stream margins, *Journal of Geophysical Research*, *103*(B6), 111–122, 1998.

Jordan, R., and J. Stark, Capillary Tension in Rotting Ice Laters, *Tech. rep.*, Technical Report ERDC/CRREL TR-01-13. US Army Corps of Engineers, Cold Regions Research and Engineering Laboratory, 2001.

Joughin, I., S. Tulaczyk, R. Bindschadler, and S. F. Price, Changes in West Antarctic Ice Stream velocities: Observation and analysis, *Journal of Geophysical Research*, *107*(B11), doi:10.1029/2001JB001029, 2002.

Joughin, I., D. R. MacAyeal, and S. Tulaczyk, Basal shear stress of the Ross ice streams from control method inversions, *Journal of Geophysical Research*, *109*(B9), doi:10.1029/2003JB002960, 2004.

Kamb, B., Rheological nonlinearity and flow instability in the deforming bed mechanism of ice stream motion, *Journal of Geophysical Research*, *96*(B10), 16,58516,595, 1991.

Kamb, B., Basal zone of the West Antarctic Ice Streams and its role in lubrication of their rapid motion, in *The West Antarctic Ice Sheet: Behavior and Environment*, vol. 77, edited by R. B. Alley and R. A. Bindschadler, pp. 157–199, AGU, Washington, DC,

671   doi:10.1029/AR077p0157, 2001.

672   Kubo, S., K. Ohji, and K. Ogura, Analysis of creep crack-propagation on the basis of the

673   plastic singular stress-field, *Engineering Fracture Mechanics*, *11*(2), 315–329, 1979.

674   Landes, J., and J. Begley, A fracture mechanics approach to ~~fatigue~~ creep crack growth, in

675   *Mechanics of Crack Growth*, pp. 128–148, Amer. Soc. for Testing and Materials (ASTM),

676   Special Technical Publication (STP) 590, Philadelphia, 1976.

677   Lliboutry, L., Temperate ice permeability, stability of water veins and percolation of

678   internal meltwater, *Journal of Glaciology*, *42*(141), 201–211, 1996.

679   MacAyeal, D. R., Large-scale ice flow over a viscous basal sediment: Theory and applica-

680   tion to Ice Stream B, Antarctica, *Journal of Geophysical Research*, *94*(B4), 4071–4087,

681   1989.

682   McMeeking, R., and R. Johnson, On the mechanics of surging glaciers, *Journal of Glaciol-*

683   *ogy*, *32*(110), 120–132, 1986.

684   Perol, T., and J. R. Rice, Control of the width of West Antarctic ice streams by internal

685   melting in the ice sheet near the margins, abstract C11B-0677 presented at 2011 Fall

686   Meeting, AGU, San Francisco, Calif., 5-9 Dec., 2011.

687   Perol, T., and J. R. Rice, Control on the width of active siple coast ice streams by internal

688   melting at their margins, in revision for submission to *Journal of Geophysical Research*,

689   2014.

690   Rathbun, A., C.Marone, R. Alley, and S. Anandakrishnan, Laboratory study of the

691   frictional rheology of sheared till, *Journal of Geophysical Research*, *113*(F02020),

692   doi:10.1029/2007JF000815, 2008.

Raymond, C., Shear margins in glaciers and ice sheets, *Journal of Glaciology*, *42*(140), 90–102, 1996.

Raymond, C., Energy balance of ice streams, *Journal of Glaciology*, *46*(155), 665–674, 2000.

Rice, J., Stresses due to a sharp notch in a work hardening elastic-plastic material loaded by longitudinal shear, *Journal of Applied Mechanics*, *34*, 287–298, 1967.

Rice, J., A path independent integral and the approximate analysis of strain concentration by notches and cracks, *Journal of Applied Mechanics*, *35*, 379–386, 1968a.

Rice, J., Mathematical analysis in the mechanics of fracture, in *Fracture: An Advanced Treatise: Vol. 2, Mathematical Fundamentals*, edited by H. Liebowitz, pp. 191–311, Academic Press, N.Y., 1968b.

Rose, K., Characteristics of ice flow in Marie Byrd Land, Antarctica, *Journal of Glaciology*, *24*, 63–75, 1979.

Scambos, T., K. Echelmeyer, M. Fahnestock, and R. Bindschadler, Develoment of enhanced ice flow at the southern margin of Ice Stream D, Antarctica, *Annals of Glaciology*, *20*, 313–318, 1994.

Schofield, A., and P. Wroth, *Critical state soil mechanics*, McGraw-Hill London, 1968.

Schoof, C., On the mechanics of ice-stream shear margins, *Journal of Glaciology*, *50*(169), 208–218, 2004.

Schoof, C., Thermally driven migration of ice-stream shear margins, *Journal of Fluid Mechanics*, *1*(1), 1–28, 2012.

Shabtaie, S., and C. Bentley, West Antarctic Ice Streams Draining into the Ross Ice Shelf: Configuration and Mass Balance, *Journal of Geophysical Research*, *92*, 1311–1336, 1987.

716 Shabtaie, S., and C. Bentley, Ice-thickness map of the west antarctic ice streams by radar

717   sounding, *Ann. Glaciol.*, *11*, 126–136, 1988.

718 Spikes, V. B., G. S. Hamilton, S. A. Arcone, S. Kaspari, and P. A. Mayewski, Variabil-

719   ity in accumulation rates from gpr profiling on the west antarctic plateau, *Annals of*

720   *Glaciology*, *39*(1), 238–244, 2004.

721 Tulaczyk, S., Ice sliding over weak, fine-grained tills: dependence of ice-till interactions

722   on till granulometry, *Geological Society of America Special Papers*, *337*, 159–177, 1999.

723 Tulaczyk, S., B. Kamb, R. P. Scherer, and H. F. Engelhardt, Sedimentary processes at

724   the base of a West Antarctic ice stream; constraints from textural and compositional

725   properties of subglacial debris, *Journal of Sedimentary Research*, *68*(3), 487–496, 1998.

726 Tulaczyk, S., W. B. Kamb, and H. Engelhardt, Basal mechanics of Ice Stream B, West

727   Antarctica 1. till mechanics, *Journal of Geophysical Research*, *105*(B1), 463–481, doi:

728   10.1029/1999JB900329, 2000.

729 Vogel, S. W., S. Tulaczyk, B. Kamb, H. Engelhardt, F. D. Carsey, A. E. Behar,

730   A. L. Lane, and I. Joughin, Subglacial conditions during and after stoppage of an

731   Antarctic Ice Stream: Is reactivation imminent?, *Geophysical Research Letter*, *32*,

732   doi:10.1029/2005GL022563, 2005.

733 Vornberger, P., and I. Whillans, Crevasse deformation and examples from ice stream b,

734   antarctica, *Journal of Glaciology*, *36*(122), 3–10, 1990.

735 Whillans, I., and C. Van Der Veen, New and improved determinations of velocity of Ice

736   Streams B and C, West Antarctica, *Journal of Glaciology*, *39*, 483–490, 1993.

737 Whillans, I., and C. Van der Veen, Transmission of stress between an ice stream and

738   interstream ridge, *Journal of Glaciology*, *47*(158), 433–440, 2001.

[739] Zotikov, I., *The Thermophysics Of Glaciers*, D. Reidel, Mass, 1986.

Appendix A: Numerical methodology

⁷⁴⁰ Our numerical implementation uses centered finite-differences on a Cartesian grid, yield-

⁷⁴¹ ing a second-order accurate approximation to the governing equations. Our grid setup

⁷⁴² allows for three refinement levels in the vicinity of the singularity at the transition point

⁷⁴³ between stream and ridge in the mechanical model (see Section 2.1). We do not use grid

⁷⁴⁴ refinement in our solution to the thermal model (see Section 2.3) because our temperature

⁷⁴⁵ field is capped at the melting point, which implies constant temperature in the vicinity

⁷⁴⁶ of the stress singularity.

⁷⁴⁷ We solve the mechanical and thermal models iteratively by repeating the following

⁷⁴⁸ computational steps: First, we seek an approximate solution to our mechanical model

⁷⁴⁹ (eq. 1). Second, we compute the dissipative heating associated with the estimated velocity

⁷⁵⁰ field and interpolate it to coincide with the temperature grid. Third, we compute the

⁷⁵¹ temperature field resulting from this dissipative heating term by solving eq. 10. Fourth,

⁷⁵² we update our estimates for the effective viscosity, thermal conductivity and specific heat

⁷⁵³ based on the new temperature field. Once the coupled mechanical and thermal models

⁷⁵⁴ have converged to a stable solution for the temperature and velocity fields of the stream-

⁷⁵⁵ ridge system, we estimate melt production (eq. 16).

⁷⁵⁶ Solving our thermal model (eq. 10) requires an iterative procedure in itself because the

⁷⁵⁷ extent of the temperate zone depends on temperature. At each iteration, we update the

⁷⁵⁸ source term based on the revised estimate for the extent of the temperate zone. We also

⁷⁵⁹ shift the transition between the boundary condition at the base of the domain such that

⁷⁶⁰ geothermal heat flux is imposed only underneath the portion of the ridge that is frozen

⁷⁶¹ (although we continue to maintain a no-slip condition underneath the entire ridge). We

762 construct two Heaviside distributions, the first representative of the temperate zone and

763 the second representative of the crevassed zone as described in Section 2.5. In both cases,

764 we use a standard trigonometric taper to regularize the Heaviside distribution. We solve

765 eq. 10 through a multigrid solver [*Briggs et al.*, 2000] in which we cycle through a hierarchy

766 of four grids. We have also found satisfactory results with classical iterative techniques

767 such as successive overrelaxation, but the multigrid is computationally more efficient and

768 less prone to error oscillations, particularly along the bed.

769   An important concern when solving our mechanical model numerically for a creep-type

770 rheology is to sufficiently resolve the singularity at the base between stream and ridge. To

771 validate our computational approach, we benchmark it against an approximate analytic

772 result valid for very wide ice streams with a temperature-independent viscosity sliding

773 over a stress-free bed. Our analytic derivation is based on the insight that the transition

774 from a slipping ice stream to a locked ridge is analogous to a crack problem. In this

775 analogy, the singularity at the bed between stream and ridge represents the crack tip and

776 the base of the ice stream can be thought of as a shear crack. Using this parallel, we can

777 study the dissipation in the near-tip field with the analytical techniques developed for

778 crack mechanics.

779   Our strategy for solving for the stress, strain-rate and dissipation in the near-tip field

780 consists of two steps: First, we can deduce from *Rice* [1967], reinterpreted for nonlinear

781 viscous flow, and *Rice* [1968b] that the shear heating in the near-tip region is given by

782
$$2\tau_E \dot{\epsilon}_E = \frac{3 J_{tip}}{2\pi r} \left(\sqrt{4 - \sin^2 \theta} + \cos \theta \right) , \tag{A1}$$

783   where r and θ are the polar coordinates centered on the slip singularity such that r is

784   the radial distance from the slip singularity and θ the angle taken to be zero at the bed

785   underneath the ridge (see Appendix B for details). Second, we derive an approximate

786   estimate of the unspecified constant, J_{tip} in eq. A1, which captures the intensity of

787   straining at the crack tip due to far-field loading, using the path-independence of J-type

788   integrals as detailed in Appendix C. We estimate J_{tip} as

$$J_{tip} = H\tau_{lat}\dot{\epsilon}_{lat}\,, \tag{A2}$$

790   where τ_{lat} is the average shear stress, τ_{xy}, at the margin that would balance the gravita-

791   tional load of the ice stream and $\dot{\epsilon}_{lat}$ is the strain rate associated with that average lateral

792   shear stress. Note that contrary to the exact result for the near-tip field (see eq. A1),

793   the evaluation of the J-integral in eq. A2 is approximate and based on the simplifying

794   assumptions that (1) the rheological behavior of ice is independent of position, hence

795   neglecting the effect of temperature variations and (2) ice streams are much wider than

796   thick $(H \ll W)$.

797   It is unreasonable to expect the numerical and analytical solutions to match exactly for

798   two reasons: First, the analytical solution is an approximate result that applies strictly

799   only to very wide ice streams. We can still use it to benchmark our computational

800   technique, however, by verifying that the error between analytical and numerical results

801   decreases with increasing ice-stream width. Second, the analytical treatment only captures

802   the contribution to shear heating that results from the stress singularity at the bed. The

803   effect of the nonsingular, but still intense, shear heating throughout the entire depth extent

804   of the ice is not accounted for by the singular term only. The numerically estimated

shear heating will thus never agree exactly with the analytical estimate, but the error

should be smallest in the immediate vicinity of the singularity $(r \rightarrow 0)$ and increase

with increasing distance. To ensure comparability between our numerical model and the

analytical benchmark results, we neglect crevassing, the temperature-dependence of the

ice rheology and thermal conductivity and the advection terms for all computations in

this section. We also assume zero basal stress underneath the ice stream.

Figure 11A confirms that the percentage error between the numerical and the analytical

estimates for the non-singular dissipation, $2\tau_E\dot{\epsilon}_E \times r$ at $\theta = 0°$, decreases with increasing

ice-stream width. To isolate the asymptotic effect of ice-stream width, all computations

were performed at the same grid resolution of $0.1\,\mathrm{m}$ in the vicinity of the singularity.

The flattening of the error curve in Figure 11A indicates that ice-streams with widths of

about $100\,H$ are well approximated by the assumption of a very wide stream and suggests

that the remaining error is dominated by the finite resolution of our computations. In

Figure 11B, we demonstrate that the percentage error between numerical and analytical

results for an ice stream of $W = 80\,H$ at $\theta = 0°$ drops well below 1% for grid resolutions

of $< 0.1\,\mathrm{m}$, highlighting that we can accurately reproduce the analytical behavior with a

sufficiently refined grid.

Beyond serving as a benchmark, the comparison between analytical and numerical re-

sults also allows us to verify if and when the far-field contribution to shear heating starts

dominating the total dissipation in the shear margin. Figure 12 shows that for a wide ice

stream with $W = 80\,H$ and a fine-grid resolution of $0.1\,\mathrm{m}$, the far-field contribution to

shear heating already becomes important at radial distances of just a few meters, render-

ing the analytical solution that only captures heating in the near-field of the singularity

828 less adequate. As the radius approaches zero, however, the numerical solutions become

829 increasingly dominated by numerical errors associated with the quickly diverging stresses

830 and are less reliable. As demonstrated in Figure 11B, the singularity can be captured

831 more accurately with sufficient computational expense, but ultimately there will always

832 be a finite, if vanishingly small, radius below which the analytical result is more accurate.

Appendix B: The near-tip field parametrized by J_{tip}

833 By reinterpreting the material rheology, a parallel can be drawn between the down-

834 stream velocity profile in a two-dimensional margin and an anti-plane crack problem. In

835 an elastic (or "deformation theory" elastic-plastic) body, the stress depends on the strain,

836 while in the viscous material considered here the stress depends on the strain rate. The

837 stress fields in the elastic and viscous problems are identical. Strain rate in the viscous

838 problem is analogous to strain in the elastic problem and downstream velocity is analogous

839 to displacement.

840 In this section, we will solve analytically for the shear heating profile near the point

841 where the bed transitions from slipping to locking. To develop the analytic solution, we

842 must neglect the temperature dependence of the rheology and assume a relationship of

843 the form

$$\dot{\epsilon}_E = A\tau_E^n, \tag{B1}$$

845 where A and n are constant. Our problem is now mathematically equivalent to the anti-

846 plane crack problem solved in *Rice* [1967, 1968b], which solved for the stress field in a

847 material with a linear stress-strain relationship up to a given yield stress and an arbitrary

848 nonlinear stress-strain relationship (including a power-law relationship as a special case)

above the yield stress. The solution in *Rice* [1967] relies on a transformation to the hodo-

graph plane. This transformation interchanges the dependent and independent variables,

allowing us to solve for y and z as a function of the strain rate components $\dot{\epsilon}_{xz}$ and $\dot{\epsilon}_{yz}$.

As shown in *Rice* [1967], the solution for the field near the crack tip takes the form

$$y = X(\dot{\epsilon}_E) + F(\dot{\epsilon}_E)\cos 2\phi \quad \text{and} \quad z = F(\dot{\epsilon}_E)\sin 2\phi\,, \tag{B2}$$

where we have used the polar coordinates

$$\dot{\epsilon}_{xy} = -\dot{\epsilon}_E \sin\phi \quad \text{and} \quad \dot{\epsilon}_{xz} = \dot{\epsilon}_E \cos\phi. \tag{B3}$$

For the power-law rheology given in equation (B1) the functions $X(\dot{\epsilon}_E)$ and $F(\dot{\epsilon}_E)$ are

$$F(\dot{\epsilon}_E) = \frac{J_{tip}}{2\pi\dot{\epsilon}_E\tau_E(\dot{\epsilon}_E)} \quad \text{and} \quad X(\dot{\epsilon}_E) = \frac{n-1}{n+1}F(\dot{\epsilon}_E), \tag{B4}$$

where the constant J_{tip} is determined by the far-field loading on the margin, and the

evaluation of J_{tip} will be discussed in detail in Appendix C. The function $F(\dot{\epsilon}_E)$ can then

be related to the shear-heating rate through

$$2\tau_E\dot{\epsilon}_E = \frac{J_{tip}}{\pi F(\dot{\epsilon}_E)}. \tag{B5}$$

To solve for $F(\dot{\epsilon}_E)$, we first eliminate ϕ from eq. B2, which uncovers the equation for a

circle

$$(y - X(\dot{\epsilon}_E))^2 + z^2 = F(\dot{\epsilon}_E)^2. \tag{B6}$$

Thus, lines of constant shear heating form circles in the (y, z)-plane with a radius of $F(\dot{\epsilon}_E)$

and a center at $y = X(\dot{\epsilon}_E), z = 0$.

For a Newtonian rheology $(n = 1)$, $X(\dot{\epsilon}_E) = 0$ and thus eq. B6 simplifies to

$$2\tau_E\dot{\epsilon}_E = \frac{J_{tip}}{\pi r}, \tag{B7}$$

where $r = \sqrt{y^2 + z^2}$. This means that lines of constant frictional heating form circles

about the point where the bed transitions from slipping to locking. Consequently, the

shear heating within the ridge and the ice stream is the same. For the more realistic

Glen's Law $(n = 3)$, the solution is more complicated. In this case, $X(\dot{\epsilon}_E) = F(\dot{\epsilon}_E)/2$ and

therefore eq. B6 is a quadratic equation in $F(\dot{\epsilon}_E)$. Noting that $F > 0$ is required for a

physically relevant frictional heating profile, the only solution is

$$F(\dot{\epsilon}_E) = \frac{2}{3} \left(\sqrt{4y^2 + 3z^2} - y \right). \tag{B8}$$

This can be simplified by using polar coordinates centered on the transition point,

$$y = r \cos \theta \quad \text{and} \quad z = r \sin \theta \tag{B9}$$

leading to the final from of the frictional heating profile

$$2\tau_E \dot{\epsilon}_E = \frac{3J_{tip}}{2\pi r} \left(\sqrt{4 - \sin^2 \theta} - \cos \theta \right). \tag{B10}$$

For Glen's law, the circles that show the lines of constant shear heating are no longer

centered on the transition point, but are shifted towards the ridge by an amount $X(\dot{\epsilon}_E) =$

$J_{tip}/(4\pi\tau_E\dot{\epsilon}_E)$ that varies with the magnitude of shear heating. This means that the shear

heating is skewed, with more intense heating in the ridge than in the ice stream.

Appendix C: J-integral evaluation for an anti-plane flow

In this section, we use a path independent integral to evaluate the constant J_{tip} from

Appendix B, linking the far-field loading on the ice stream to the shear heating singularity

near the transition from a slipping to a locking bed. This is an extension to J-type

integrals, which were pioneered by *Rice* [1968a], *Rice* [1968b], *Cherepanov* [1968] and *Bilby*

and Eshelby [1968] in the context of cracks in elastic solids, but have been generalized to more complex, nonlinear creep rheologies (e.g. *Goldman and Hutchinson* [1975]; *Landes and Begley* [1976]; *Kubo et al.* [1979]; *Ben Amar and Rice* [2002]) relevant for our case and applied to glaciers by *McMeeking and Johnson* [1986].

Our domain of ice is made to coincide with that of a classical anti-plane crack problem, for an ice slab of thickness $2H$, when we add to our domain its mirror image about the base. We thus have a classical crack problem, with $u = 0$ along the prolongation of the slipping zone into the locked zone $z = 0$ and $y > 0$, gravity loadings in the respective domains $z > 0$ and $z < 0$, traction-free surfaces, $\tau_{zx} = 0$, at $z = \pm H$ and with $\tau_{zx} = \tau_{base}$ on both sides of $z = 0$ where $y < 0$.

Assuming that the properties of ice do not change with temperature (or that temperature varies only with z), the appropriate path-independent integral for our problem is

$$J = \int_{\Gamma} \left(\Phi(\dot{\epsilon}_E, z) - \rho g \sin \alpha \, u \right) \mathrm{d}z - \boldsymbol{\tau} \cdot \mathbf{n} \frac{\partial u}{\partial y} \mathrm{d}s, \tag{C1}$$

where $\boldsymbol{\tau} = (\tau_{xy}, \tau_{xz})$, Φ is analogous to the strain energy density function from elasticity and is defined for a creeping solid as

$$\Phi(\dot{\epsilon}_E) = 2 \int_0^{\dot{\epsilon}_E} \tau_E(\xi) \, \mathrm{d}\xi \tag{C2}$$

$\mathbf{n}$ is the outward unit normal to the curve Γ, and $\mathrm{d}s$ is evaluated in a counter-clockwise fashion. For any closed curve Γ that does not enclose the transition point (i.e., the crack tip), $J = 0$ so that the integral is path-independent.

For classical crack problems, Γ is taken to start on the lower crack surface $z = 0^-$, $y < 0$, encircle the crack tip and end on the upper crack surface $z = 0^+$, $y < 0$. J is

910 independent of path Γ for all paths with the same starting and ending points. If there

911 is no traction on the crack faces ($\tau_{base} = 0$), J is independent of where we start and end

912 along the faces. When $\tau_{base} \neq 0$, we start and end at a point close to the tip on the crack

913 face where $y < 0$. Then we take the limit $y \to 0$ on both faces and define J_{tip} as the value

914 of J. Subsequently, we focus on the part of any path Γ in the domain $z \geq 0$ so that the

915 result of eq. C1, taken along that part of the path, is $J_{tip}/2$.

916   We now evaluate J_{tip} along the two curves Γ_{tip} and Γ_{far} shown in Figure 13, which meet

917 these specifications, with Γ_{tip} sufficiently close to the transition point that the deformation

918 can be described by the solution in Appendix B. Evaluation along Γ_{tip} just confirms

919 the relations involving J_{tip} in that appendix. For a typical ice-stream geometry, the

920 contribution to J from the portion of Γ_{far} in the center of the ridge is negligible, so for

921 the boundary conditions highlighted in Figure 13

922
$$\frac{J_{tip}}{2} = \int_H^0 \left[\Phi\left(\dot{\epsilon}_{xz}\right) - \rho g \sin\alpha \, u \right]_{y=-W/2} \mathrm{d}z + \int_{-W/2}^0 \tau_{base} \frac{\partial u(y,0)}{\partial y} \mathrm{d}y. \qquad (C3)$$

923 To calculate the two integrals in eq. C3, we need to know u within the ice stream. An

924 approximate evaluation can be produced using a simple one-dimensional model with a

925 constant basal stress τ_{base} beneath the ice stream. Assuming that τ_{xy} and u are functions

926 of y alone, we integrate the equation for mechanical equilibrium from $z = 0$ to $z = H$,

927 arriving at

928
$$\frac{\mathrm{d}\tau_{xy}}{\mathrm{d}y} = -\left(\rho g \sin\alpha - \frac{\tau_{base}}{H} \right) \quad \text{and} \quad \dot{\epsilon}_{xy} = A\tau_{xy}^n, \qquad (C4)$$

929 where it may be noted that the first of these is exact if we reinterpret τ_{xy} as its average

930 over the thickness H in the z direction. This average becomes arbitrarily larger than the

931 average of τ_{xz} as W/H becomes increasingly large. In that same limit, $\dot{\epsilon}_{xy}$ becomes much

larger than $\dot{\epsilon}_{xz}$, and the flow law reduces to the second equation. Treating the problem in

that large W/H limit, we integrate outwards from the stress free boundary at $y = -W/2$

to calculate $\tau_{xy}(y)$ and hence the strain-rate profile

$$\frac{\mathrm{d}u}{\mathrm{d}y} = -2A \left(\rho g \sin \alpha - \frac{\tau_{base}}{H}\right)^n \left(y + \frac{W}{2}\right)^n. \tag{C5}$$

To create the single boundary condition needed to integrate this equation, we assume that

the downstream velocity vanishes at the margin, as is appropriate to the large W/H limit,

and find

$$u = \frac{2A}{n+1} \left(\rho g \sin \alpha - \frac{\tau_{base}}{H}\right)^n \left[\left(\frac{W}{2}\right)^{n+1} - \left(y + \frac{W}{2}\right)^{n+1}\right]. \tag{C6}$$

The boundary condition used here is an approximation since the velocity field in the

vicinity of the margin will be a function of both y and z and will not completely vanish.

However, comparing the predictions for velocity in the center of the ice stream from eq. C6

and two-dimensional computational models, we find that in the limit $H \ll W/2$, eq. C6

is the asymptotic limit of such models.

Using the one-dimensional model to evaluate J_{tip}, which relies only on the value of u at

the center of the ice stream, eq. C3 gives:

$$\frac{J_{tip}}{2} = \frac{2AH}{n+1} \left(\rho g \sin \alpha - \frac{\tau_{base}}{H}\right)^{n+1} \left(\frac{W}{2}\right)^{n+1} \tag{C7}$$

Defining the average lateral shear stress at the margins and the corresponding equivalent

strain rate

$$\tau_{lat} = \left(\rho g \sin \alpha - \frac{\tau_{base}}{H}\right) \frac{W}{2} \quad \text{and} \quad \dot{\epsilon}_{lat} = A\tau_{lat}^n, \tag{C8}$$

we can simplify the equation for J_{tip} to

$$J_{tip} = \frac{4H}{n+1} \tau_{lat} \dot{\epsilon}_{lat} \tag{C9}$$

953   when $W \gg H$.

Tables

Table 1.   Overview of the notation used in this study.

Symbol	Variable	Unit
a	surface accumulation rate of ice	$\mathrm{m\,yr^{-1}}$
A	temperature-dependent creep parameter	$\mathrm{s^{-1}\,Pa^{-3}}$
α	inclination angle	rad
c	specific heat of ice	$\mathrm{J\,kg^{-1}\,K^{-1}}$
c_1	empirical forefactor	$\mathrm{J\,kg^{-1}\,K^{-1}}$
c_2	empirical forefactor	$\mathrm{J\,kg^{-1}\,K^{-2}}$
d	grain size	mm
E	enhancement factor	
$\boldsymbol{\dot{\epsilon}}$	strain rate tensor	$\mathrm{yr^{-1}}$
$\dot{\epsilon}_D$	strain resulting from diffusional creep	$\mathrm{yr^{-1}}$
$\dot{\epsilon}_E$	effective strain rate	$\mathrm{yr^{-1}}$
$\dot{\epsilon}_G$	strain resulting from Glen's Law	$\mathrm{yr^{-1}}$
$\dot{\epsilon}_{lat}$	average shear strain at the margin	$\mathrm{yr^{-1}}$
F	variable used to calculate transition point stress field	m
g	gravitational acceleration	$\mathrm{m\,s^{-2}}$
G	Geothermal heat flux at the ice sheet base	$\mathrm{m\,W\,m^{-2}}$
Γ	curve along which J-integral is evaluated	
Γ_{tip}	curve through transition point stress field	
Γ_{far}	curve around border of domain	
H	ice sheet thickness	m
H_m	height of the temperate zone	m
J_{tip}	J-integral evaluated along Γ_{tip}	$\mathrm{J\,m^{-2}\,yr^{-1}}$
k	thermal conductivity of ice	$\mathrm{W\,m^{-1}\,K^{-1}}$
k_1	empirical factor	$\mathrm{W\,m^{-1}\,K^{-1}}$
k_2	empirical factor	$\mathrm{K^{-1}}$
k_B	Boltzmann constant	$\mathrm{m^2 kg\,s^{-2}\,K^{-1}}$
L	latent heat per unit mass	$\mathrm{J\,kg^{-1}}$
$\dot{m}$	melt rate per unit volume	$\mathrm{kg\,s^{-1}\,m^{-3}}$
n	exponent in ice rheology	
$\mathbf{n}$	unit normal vector to Γ	
μ	effective viscosity of ice	$\mathrm{Pa\,s}$
μ_w	viscosity of water	$\mathrm{Pa\,s}$
Ω	molecular volume	$\mathrm{m^3}$
ϕ	angle between principal strain rate direction and z	rad
Φ	strain energy density analog	$\mathrm{Pa\,yr^{-1}}$
q	meltwater flux	$\mathrm{m\,s^{-1}}$
q_{base}	meltwater flux at the bed	$\mathrm{m\,s^{-1}}$
q_{temp}	meltwater flux in the temperate zone	$\mathrm{m\,s^{-1}}$
Q	activation energy	$\mathrm{J\,mol^{-1}}$

Symbol	Variable	Unit
r	radial distance from the singularity	m
R	gas constant	$\mathrm{J\,K^{-1}\,mol^{-1}}$
ρ	density of ice	$\mathrm{kg\,m^{-3}}$
ρ_w	density of water	$\mathrm{kg\,m^{-3}}$
s	arc length of curve Γ	m
T	temperature	C
T_{melt}	melting temperature of ice	C
T_h	temperature adjusted for melting point depression	K
T^*	cutoff temperature in Glen's Law	K
$\boldsymbol{\tau}$	stress tensor	Pa
τ_E	effective stress	Pa
τ_{lat}	average shear stress at the margin	Pa
τ_{base}	basal shear stress	Pa
θ	angle from the base of the ridge	rad
u	downstream velocity component	$\mathrm{m\,s^{-1}}$
v	transverse velocity component	$\mathrm{m\,s^{-1}}$
v_0	speed of lateral margin migration	$\mathrm{m\,s^{-1}}$
v_{out}	velocity boundary condition in local model	$\mathrm{m\,s^{-1}}$
w	vertical velocity component	$\mathrm{m\,s^{-1}}$
W	ice stream width	m
x	downstream cartesian coordinate	m
X	variable used to calculate transition point stress field	m
ξ	dummy integration variable used to define Φ	
y	transverse cartesian coordinate	m
z	vertical cartesian coordinate	m

Figures

A. Satellite image of Dragon margin

B. Surface crevassing and borehole locations
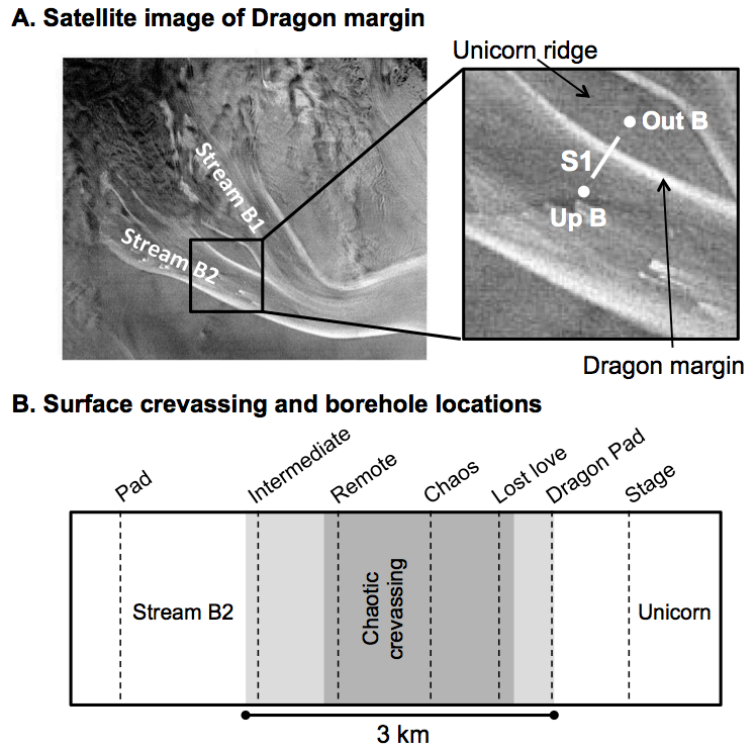
Figure 1.   A: The left panel shows a satellite image of the confluence between ice streams B1 and B2 in the upstream portion of Whillans Ice Stream, taken by the Radarsat Antarctic Mapping Project. The right panel is a detailed view of Dragon margin, Unicorn ridge and the profile S1 along which *Echelmeyer and Harrison* [1999] measured surface velocities and *Harrison et al.* [1998] reported temperature for the upper few hundred meters. We have highlighted the positions of the two outermost boreholes, "Out B" and "Up B", used in *Harrison et al.* [1998]. B: Approximate locations of the seven boreholes in the vicinity of the shear margin with respect to surface crevassing (after *Harrison et al.* [1998]). The dark grey area represents the roughly 2 km-wide zone of chaotic crevassing. The light grey zones exhibit less intense crevassing.
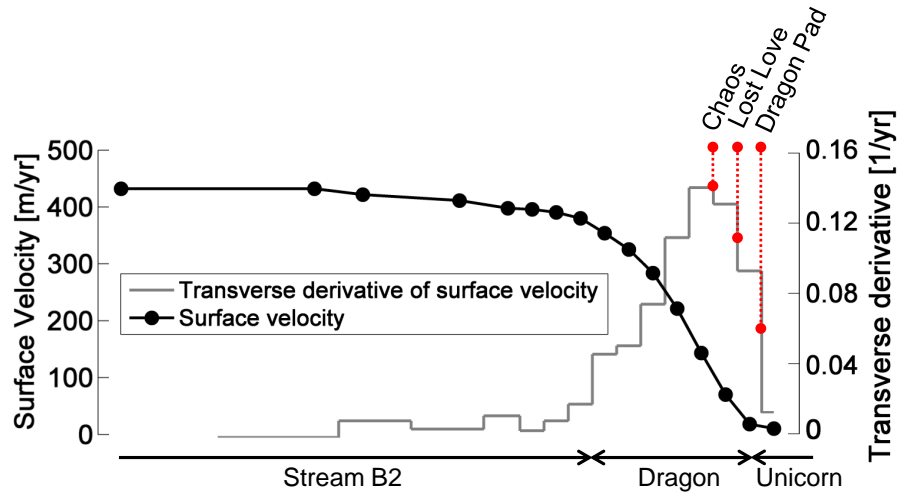
Figure 2. Surface velocities across Dragon margin as measured by *Echelmeyer and Harrison* [1999] and the transverse derivative of surface velocities, du/dy, computed from the measured surface velocities. Highlighted in red are the approximate transverse velocity derivatives for boreholes "Dragon Pad", "Love Love", and "Chaos" quoted from *Harrison et al.* [1998].
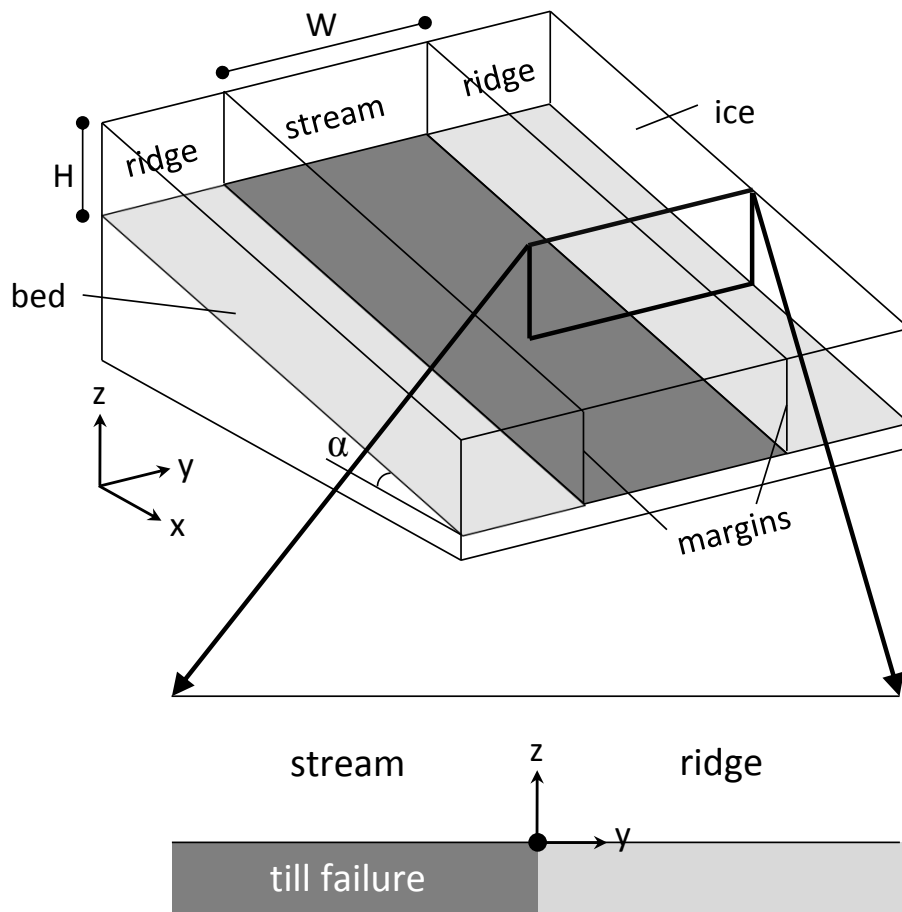
Figure 3.   Simplified geometry of our model setup. The ice thickness is H and the total width of the stream is W. The 2D setup (bottom) is equivalent to assuming a 3D stream-ridge geometry with no downstream variation (top).
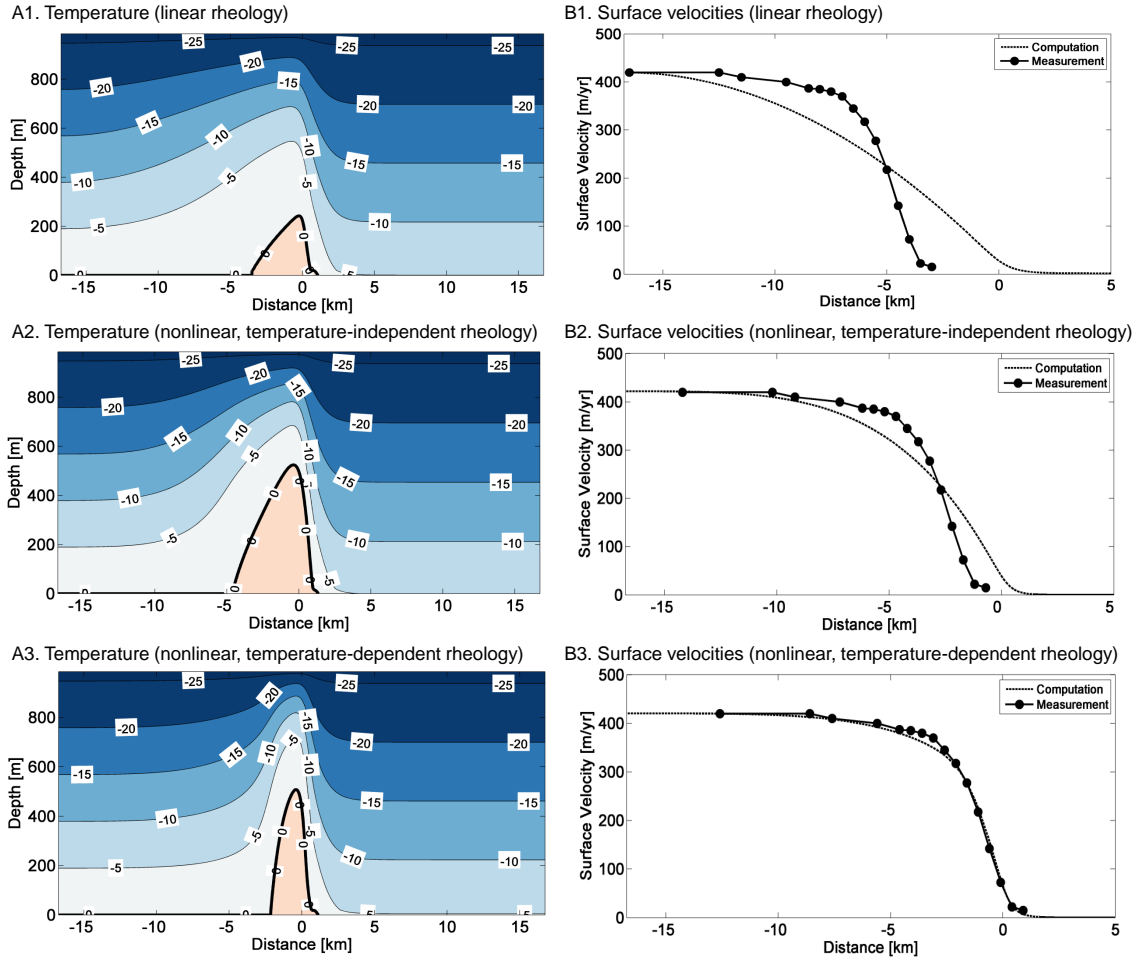
Figure 4.   Top: Temperature field (A1) and surface velocities (B1) assuming a Newtonian rheology of $\mu = 10^{14}\,\mathrm{Pa\,s}$. Middle: Temperature field (A2) and surface velocities (B2) for a power-law rheology that accounts for the strain-rate dependence of the effective viscosity, but neglects the temperature dependence. Bottom: Temperature field (A2) and surface velocities (B2) for a realistic rheology that captures both strain-rate and temperature dependence. The best fitting basal stresses are $\tau_{base} = 2.56\,\mathrm{kPa}$ (A1, B1), $\tau_{base} = 1.12\,\mathrm{kPa}$ (A2, B2) and $\tau_{base} = 4.07\,\mathrm{kPa}$ (A3, B3), respectively. All computations neglect advection and surface crevassing. Measured surface velocities are from *Echelmeyer and Harrison* [1999].
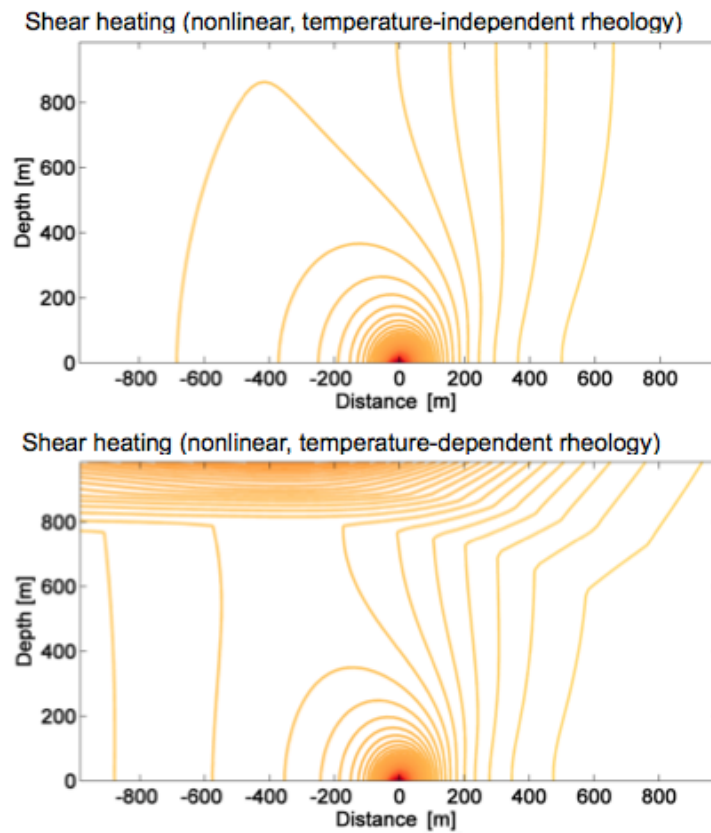
Figure 5.   Eighty contours of constant shear heating in units of [Pa/yr] in the vicinity of the singularity when neglecting (top) and including (bottom) the temperature-dependence of the rheology.
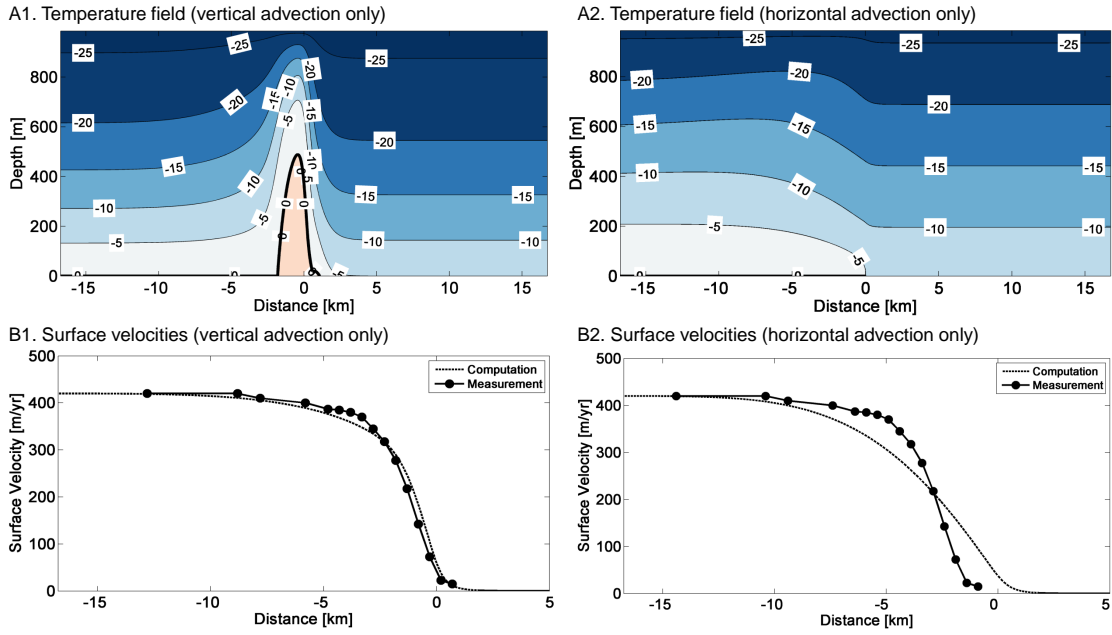
Figure 6. Temperature fields and surface velocities for Dragon margin when including only vertical advection (A1 and B1) with $a = 0.1\,\mathrm{m/yr}$ and only horizontal advection (A2 and B2) with $v = -7.3\,\mathrm{km/yr}$, respectively. The best fitting basal stresses are $\tau_{base} = 5.31\,\mathrm{kPa}$ (A1 and B1) and $\tau_{base} = 0.94\,\mathrm{kPa}$ (A2 and B2), respectively. Both computations neglect surface crevassing.
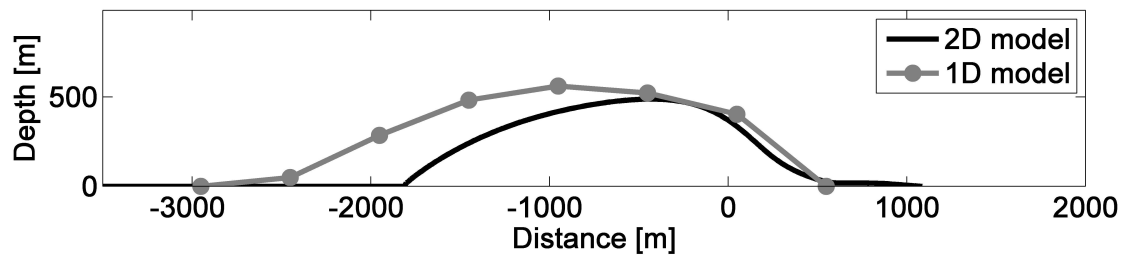
Figure 7.   Comparison of the temperate zone from Figures 6A1 and B1, replotted on a 1:1 scale, with the simplified 1D model by *Perol and Rice* [2011] using measured surface velocities *Echelmeyer and Harrison* [1999] with a surface accumulation of $a = 0.1\,\mathrm{m/yr}$ in both cases.
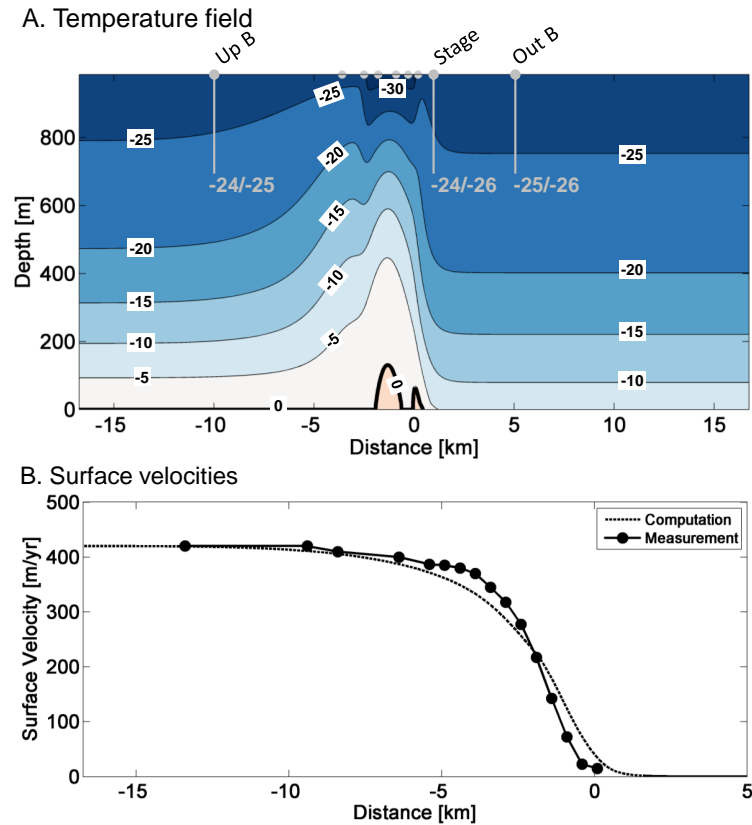
Figure 8.   Temperature field (A) and surface velocities (B) for Dragon margin when attempting to match the observed borehole temperatures [*Harrison et al.*, 1998], see Figures 1 and 2 for borehole locations, and surface velocities [*Echelmeyer and Harrison*, 1999] simultaneously. The computation is based on the model parameters $\tau_{base} = 1.22\,\text{kPa}$, accumulation $a = 0.23\,\text{m/yr}$, geothermal heat flux $G = 85\,\text{mW/m}^2$ and horizontal advection at $v = -0.35\,\text{m/yr}$. The approximate locations of the nine boreholes considered in *Harrison et al.* [1998] are indicated as grey dots. We highlight the boreholes located far from margin as grey lines in accordance with their depth. The left numbers represent the computed value and the right number the measured value at maximum depth. The corresponding temperature estimates for the boreholes in the vicinity of the margin are shown in the next figure.
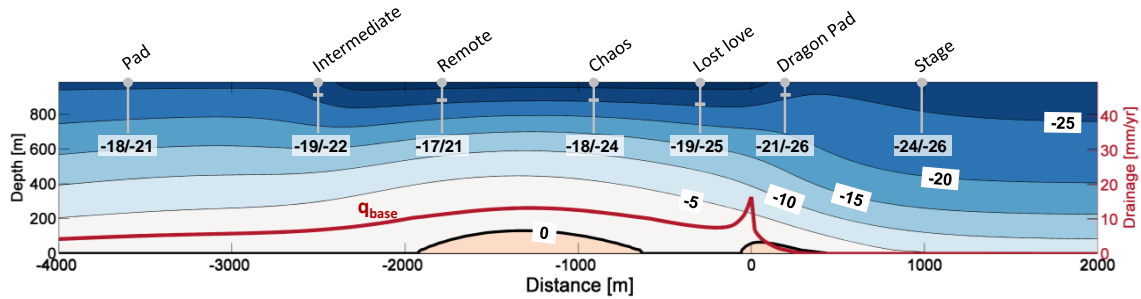
Figure 9.   Extent of a potential temperate zone at Dragon margin plotted on a 1:1 scale and meltwater flux at the base of the ice, q_{base}, in mm/yr (grey line) for the computation also shown in Figure 8. The total meltwater produced in the temperate zone is $25\,\mathrm{m^2/yr}$. The approximate locations of the boreholes from *Harrison et al.* [1998] are highlighted in grey with the left number representing the computed temperature and the right value the measured temperature at a depth of approximately $700\,\mathrm{m}$. Small horizontal dashes along the boreholes in the vicinity of the shear margin indicate the approximate position of the $-26°C$ contour.
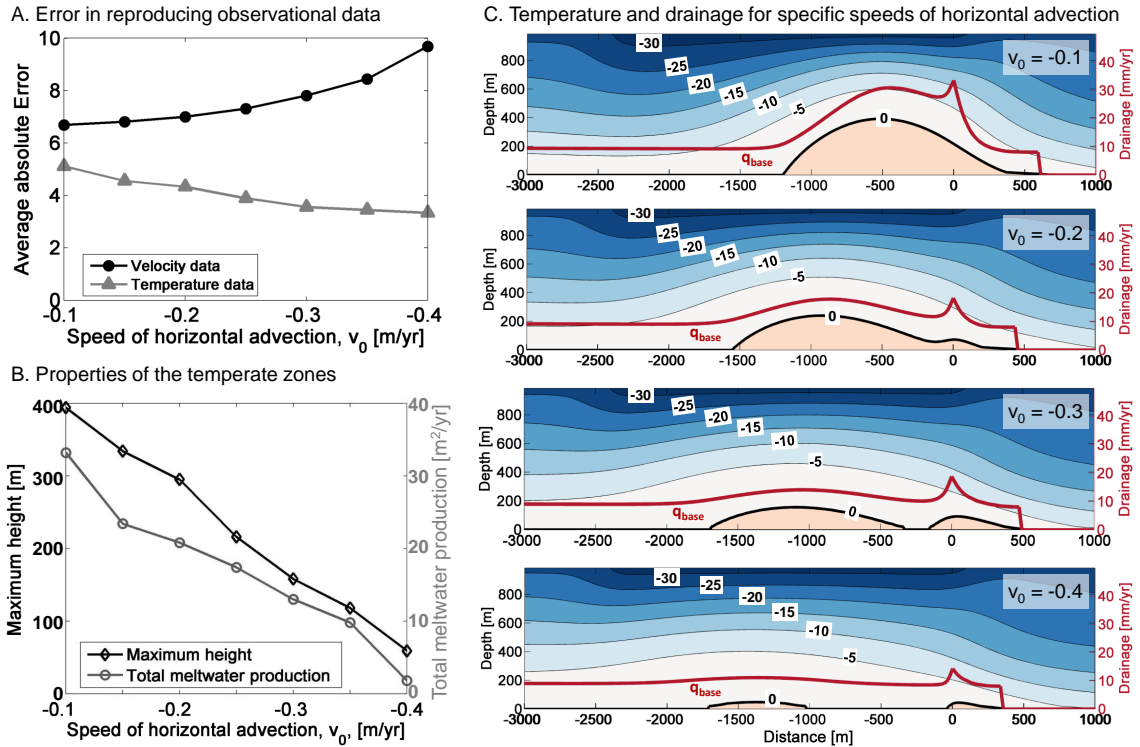
Figure 10. A. Average absolute error in reproducing observed temperatures and velocities for horizontal advection speeds between $v_0 = -0.1$ and $-0.4\,\mathrm{m/yr}$. B. Maximum height of the temperate zones and total meltwater production for horizontal advection speeds between -0.1 and $-0.4\,\mathrm{m/yr}$. The total meltwater production is computed by integrating the basal meltwater flux, q_{base}, over the width of the zone where ice is temperate not only at the bed but at finite depth. C. Temperature fields and drainage curves for the four horizontal advection speeds $v_0 = -0.1, -0.2, -0.3$ and $-0.4\,\mathrm{m/yr}$, respectively. The best-fitting basal stresses for the four computations are $\tau_{base} = 1.57, 1.44, 1.31$ and $1.13\,\mathrm{kPa}$ from the top to the bottom. Apart from the horizontal-advection speed and basal stress, all computations are based on the same model parameters, most importantly $a = 0.23\,\mathrm{m/yr}$ and $G = 85\,\mathrm{mW/m^2}$.

A. Asymptotically decreasing error with increasing width
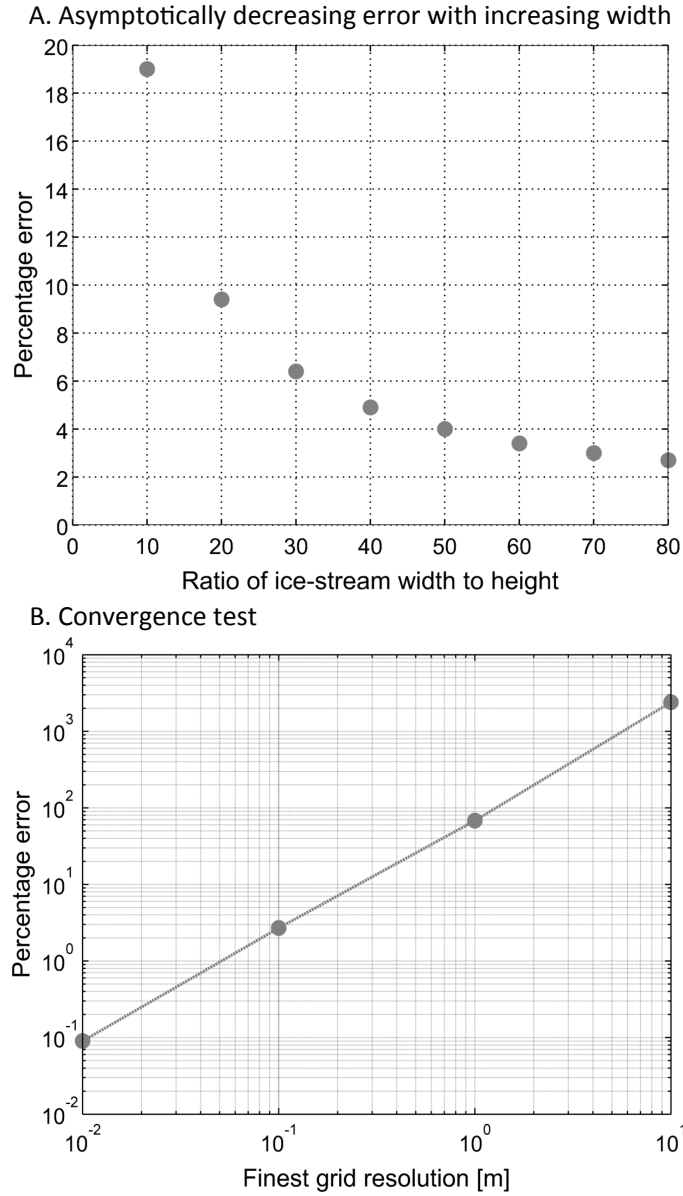
B. Convergence test

Figure 11. Validation of our computational approach. Panel A shows that the percentage error between the numerical and analytical estimates for the nonsingular shear heating, $2\tau_E \dot{\epsilon}_E \times r$, at $\theta = 0°$, decreases as the ice-stream width increases. The grid resolution in the vicinity of the singularity is $0.1\,\mathrm{m}$ for all computations. Panel B summarizes the results of a convergence test performed for a wide ice stream with $W/H \approx 80$ at $\theta = 0°$.
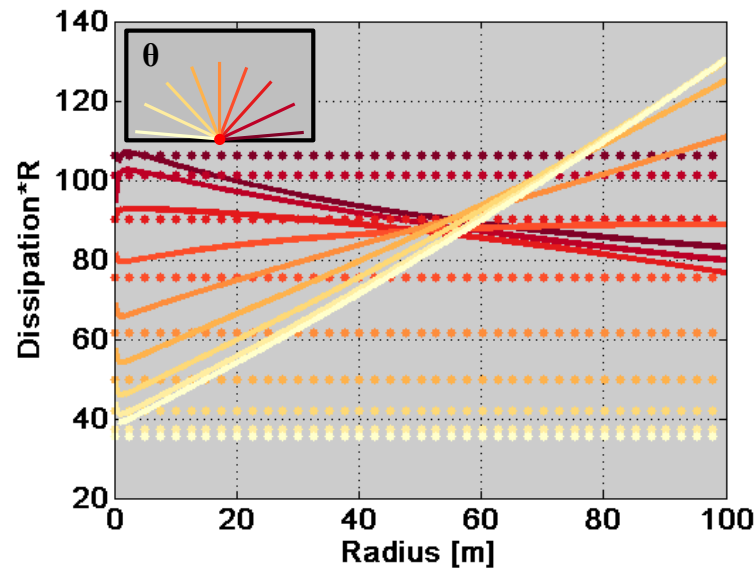
Figure 12. Plot of the angular dependence of dissipation for nine different angles from $5° - 175°$ represented by a specific color as detailed in the inlet on the upper left. For each angle, the dotted lines represent the analytic and the full lines the numeric result. Evidently, the importance of the far-field contribution to shear heating depends primarily on the distance from the singularity, but also on the angle.
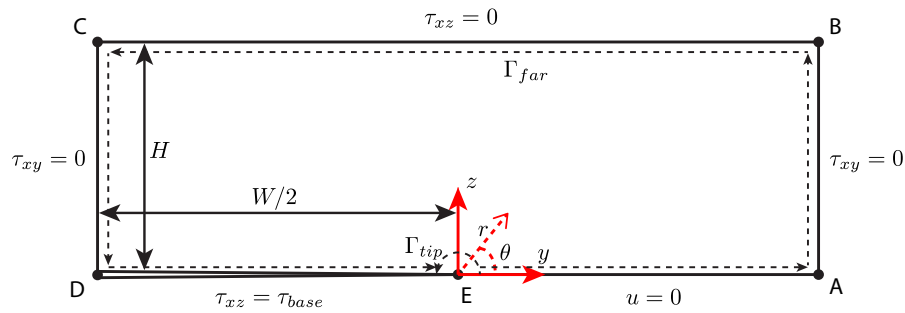
Figure 13.   Sketch showing the two paths Γ_{tip} and Γ_{far} used to evaluate the path independent integral defined in eq. C1. Γ_{tip} is taken sufficiently close to the transition point so that the stress field is described by the solution in Appendix B, and Γ_{far} is evaluated along the border of the domain.